Running Title: NMR Analysis of the KR2 H180A mutant

Structural and functional consequences of the H180A mutation of the light-driven sodium pump KR2

Clara Nassrin Kriebel,[1] Marvin Asido*,[2] Jagdeep Kaur*,[1] Jennifer Orth,[1] Philipp Braun,[1] Johanna Becker-Baldus,[1] Josef Wachtveitl,[2] and Clemens Glaubitz[1**]

[1]Institute for Biophysical Chemistry and Center for Biomolecular Magnetic Resonance (BMRZ), Goethe University Frankfurt, Max von Laue-Straße 9, 60438 Frankfurt am Main, Germany

[2]Institute for Physical and Theoretical Chemistry, Goethe University Frankfurt, Max von Laue-Straße 7, 60438 Frankfurt am Main, Germany

(*) contributed equally

(**) glaubitz@em.uni-frankfurt.de

Abstract

Krokinobacter eikastus rhodopsin 2 (KR2) is a light-driven pentameric sodium pump. Its ability to translocate cations other than protons and to create an electrochemical potential makes it an attractive optogenetic tool. Tailoring its ion pumping characteristics by mutations is therefore of great interest. In addition, understanding the functional and structural consequences of certain mutations helps to derive a functional mechanism of ion selectivity and transfer of KR2. Based on solid-state NMR spectroscopy, we report an extensive chemical shift resonance assignment of KR2 within lipid bilayers. This data set was then used to probe site-resolved allosteric effects of sodium binding, which revealed multiple responsive sites including the Schiff base nitrogen and the NDQ motif. Based on this data set, the consequences of the H180A mutation are probed. The mutant is silenced in the presence of sodium while in its absence, proton pumping is observed. Our data reveal specific long-range effects along the sodium transfer pathway. These experiments are complemented by time-resolved optical spectroscopy. Our data suggest a model in which sodium uptake by the mutant can still take place, while sodium release and backflow control are disturbed.

Statement of significance

Krokinobacter eikastus rhodopsin 2 (KR2) is a member of the microbial rhodopsin superfamily. It acts as a light-driven sodium pump but switches into a proton pumping mode in the absence of sodium. Here, a mutation is described which switches KR2 into a proton-only transfer mode. The effects of the mutation are compared to the wild type based on solid-state NMR spectroscopy, time-resolved optical spectroscopy and functional data. Understanding the effect of functional mutations helps to reveal the surprising sodium transfer properties of this rhodopsin.

Introduction

The light-driven sodium pump KR2 (*Krokinobacter eikastus rhodopsin 2*) is a microbial rhodopsin discovered in marine flavobacteria (1) with remarkable ion transfer characteristics: The outward-directed transport of Na^+ takes place across the positively charged retinal Schiff base (SB) and is associated with a photocycle and photointermediates similar to those known from proton pumps such as bacteriorhodopsin (BR) or proteorhodopsin (PR). Besides Na^+, Li^+ can be pumped outwards as well, whereas protons are only translocated in the absence of sodium or in the presence of K^+, Rb^+, Cs^+ (1).

As typical for proteins of this family, KR2 is composed of seven transmembrane helices connected by three intra- and extracellular loops (Fig. 1a). The light capturing chromophore is an all-*trans* retinal bound to the protein via a Schiff base linkage to Lys255 in helix G. KR2 forms pentameric complexes (Fig. 1b). KR2 is characterized by a specific NDQ sequence motif in helix C (N112, D116, Q123). The neutral residues N112 and Q123 are located at positions occupied by proton donors and acceptors in proton pumps such as bacteriorhodopsin (BR) or proteorhodopsin (PR) (D85/D96 and D97/E108) (2-4). D116 serves as the Schiff base counter ion. Mutation studies have demonstrated their key role in ion selectivity (1) and translocation (5,6).

A number of ground state structures obtained under acidic and neutral conditions in both monomeric and pentameric form have been reported (5-7). An outward-facing Na^+ binding site formed at the pentamer interface between the protomers was found (Fig. 1a, b) (8). Although sodium binding to this site in the ground state is not a requirement for sodium transport (1,6), this binding site might be supportive of ion translocation (9,10).

A recently published structure of the pentameric KR2 O-state (11) as well a serial crystallography study on monomeric KR2 (12) revealed a transiently formed and populated Na^+ binding site within the protein close to N112 and D116 (Fig. 1a). This finding correlates with time-resolved optical spectroscopy by which a classical photocycle with distinct intermediates has been found (Fig. 1c) and in which the O-state population seems to be correlated with the presence of NaCl (1,13).

In the dark, the protonated Schiff base (pSB) is located in the center of the ion translocation pathway where it prevents the passage of other cations. Green light absorption isomerizes the retinal from the all-*trans* to 13-*cis* conformation. Its relaxation induces the formation of a K-like state and initiates the photocycle. This state is followed by two states in equilibrium, the L- and M-like intermediates. Different to the K- , and also to the later O-like state, the M state shows not a red, but a blue-shifted absorption characteristic which originates from a deprotonated retinal Schiff base in M. Proton transfer from the Schiff base to its counter ion D116 allows

D116 to subsequently form hydrogen bonds with S70 and N112 and by that transiently eliminates the positive charge in the center of the pentameric protein. Sodium uptake seems to take place from the cytoplasmic region via S64-Q123, followed by conduction through the retinal SB cavity to the extracellular side during the transition to the O-intermediate. In the sodium-connected O-state, the proton is assumed to re-associate with the Schiff base again via D116, which prevents the backflow of the sodium ion. After the extracellular release of the sodium ion, the protein converts back to the initial ground state. Based on mutation studies, spectroscopy and structural data, a number of residues besides the retinal Schiff base (RSB), N112, D116 and Q123 have been identified to be essential for ion uptake and release (1,6,11,12,14-17). The S64-Q123 pair seems to form an important gate blocking the Na^+ entry from the ground state into the ion pathway, which runs along helices B and C. The charged cluster E11-E160-R243 at the extracellular side is either part of the release pathway and/or important for protein stability (1,5,6,11). Another pathway lined by Q78, D102, N106, R109 has also been suggested (11).

Nevertheless, details of the ion selectivity mechanism of KR2 are not fully understood yet. Besides of optical and vibrational spectroscopy (9,10,18,19), especially solid-state nuclear magnetic resonance (ssNMR) spectroscopy based on magic angle spinning (MAS) offers the possibility to link functional with structural data by performing NMR experiments directly within lipid bilayers. It has been used extensively for microbial rhodopsins (20). Photointermediates are best characterized based on light-induced cryo-trapping procedures combined with selective isotope labelling schemes and utilizing dynamic nuclear polarization (DNP)-enhanced ssNMR (21-23). However, the basis for a more global structural analysis is an extensive ^{13}C, ^{15}N resonance assignment, which has to be carried out on non-frozen samples at the highest possible magnetic fields. These conditions are usually only compatible with the protein ground state but not with photointermediates. As the acquisition of the required multidimensional MAS NMR data sets is very time-consuming, a number of experimental schemes have been developed for time-efficient data accumulation, such as non-uniform sampling (NUS) (24,25) or paramagnetic doping (26,27). Furthermore, improved magnetization transfer schemes based on optimal control (OC) have been shown to provide an additional gain in sensitivity (28). ssNMR was already successfully applied for the analysis of KR2 and its H30A mutant (29-31), which revealed long-range interactions between H30, bound sodium ions and the retinal binding pocket and indicated cross-protomer interactions within the pentamer. DNP-enhanced ssNMR on various cryo-trapped KR2 photointermediates revealed a disturbed all-*trans* retinal Schiff base complex in the O-state (21).

KR2 is of potential interest in the field of optogenetics since its cation pumping activity makes it a promising tool as a neural silencer (8,32,33). It is therefore also of interest to find factors

such as specific mutations by which its activity could be modulated. The ion selectivity and pumping behavior of the wild type and various mutants have been extensively studied (1,5,6,17,29). For example, the H30A mutation at the protomer interface abolishes KR2's proton pumping ability (Fig. 1e middle), slows down the photocycle and suppresses extracellular sodium binding (1,29). A chemical shift analysis revealed several functionally important sites as being affected by this mutation including the retinal, the Schiff base nitrogen, the Schiff base counterion D116 and T83, R243 and D251 as parts of the ion release region. These long-range perturbations are most likely caused within the pentamer across the protomer interface by disturbed interprotomer H-bond interactions (29), since the distance between H30 and the Schiff base within one protomer is longer compared to the Schiff base in the adjacent protomer. Also X-ray structures suggested previously that interactions at the oligomeric interface of KR2 influence the conformation of the retinal binding pocket (6). The crystal structure of KR2 H30A mutant (11) was found to be very similar to the wild type, including the sodium ion bound at the oligomeric interface. However, in the mutant, the original region of the H30 side chain is now filled with two additional water molecules and a second conformation of Y108 seems to appear, which was not observed in any other KR2 structure. Thus, the regions around the affected sites including residues Q78, N81, Y108, H30' and the putative ion release cavity, might be important for KR2s selectivity mechanism by being part of the ion pumping pathway (11).

Mutating also the second Histidine H180 has a strong functional effect: The λ_{max} vs. pH titration curve deviates clearly from the wild type and from the H30A mutant (Fig. 1d) but most strikingly, in the presence of NaCl, both Na^+ and H^+ transfer is abolished. In the absence of NaCl, H^+ pumping still occurs (Fig. 1e, right). This is especially surprising, since H180 in transmembrane helix E is neither located at the oligomerization interface nor in the vicinity of the retinal or of any other residue known to be directly involved in the photocycle (Fig 1a).

Here, we use solid-state NMR spectroscopy complemented by optical spectroscopy to resolve the reasons for the surprising effects of this mutation. For this purpose, we have fully assigned the KR2 wild type using 3D/4D MAS NMR experiments and compared the spectra with those of the H180A mutant. Interestingly, in contrast to H30A, key sites such as the chromophore Schiff base or residues in the NDQ motif were not affected. However, a spectral response was observed for residues within the ion transfer pathway. Our experiments are complemented by data from time-resolved optical spectroscopy which indicate that the sodium ion might be able to enter KR2 although net sodium transport is not observed.

Materials and Methods

Sample preparation

Expression and purification on wild type KR2 was carried out exactly as described previously (29). The gene for $KR2_{H180A}$ was constructed based on the wild type in the pet26b-KR2 plasmid using site-directed mutagenesis. The mutation was confirmed by DNA sequencing (SRD, Bad Homburg, Germany). KR2 and $KR2_{H180A}$ were transformed in *E. coli* C43(DE3) strain. A preculture was grown overnight in LB medium at 27°C and 320 rpm in the presence of 100 µg/ml of kanamycin. Cells from the preculture were pelleted and transferred to M9 medium (1:100 dilution). For preparing uniformly labelled [U-^{13}C,^{15}N]-KR2, selectively labelled [U-^{13}C,^{15}N, FYLIV]-KR2 and reverse labelled [U-^{13}C,^{15}N, rev-FYLIV]-KR2, the M9 medium was supplemented with ^{13}C-glucose, ^{15}N-ammonium chloride and corresponding amino acids. The culture was grown (37°C, 220 rpm) until OD_{600} reached 0.6. Protein expression was then induced with 0.5 mM isopropyl β-D-1-thiogalactopyranoside (IPTG). An amount of 7 µM of all-*trans* retinal was added. After an incubation for 16 h at 27 °C, cells were harvested and passed through a cell disruptor (Constant Systems) at 1.85 kbar. Membranes were solubilized overnight in buffer containing 1.5% (w/v) dodecyl-β-D-maltoside (DDM). The solubilized protein was purified by Ni-NTA affinity chromatography. Purity and homogeneity of the sample were verified by SDS PAGE and optical absorption spectroscopy. The protein yield was approx. 10 mg / L culture. KR2 and $KR2_{H180A}$ was reconstituted into 1,2-dimyristoyl-*sn*-glycero-3-phosphocholine (DMPC) / 1,2-dimyristoyl-*sn*-glycero-3-phosphate (DMPA) liposomes (9:1 mole/mole) at a lipid-to-protein ratio of 0.5 w/w as described before. Proteoliposomes were collected by ultracentrifugation and then resuspended in buffer containing 50 mM Tris, or 100 mM NaCl and 25 mM Tris, 5 mM $MgCl_2$ at pH 8.5. Samples were doped with 2 mM Gd-DOTA (26) and pelleted by ultracentrifugation. Prior to Gd-DOTA doping, the liposome suspensions containing 100 mM NaCl were illuminated twice for 3 min at room temperature with green light (Schott KL 1500LCD light source) in order to induce ion pumping and ion equilibration inside and outside of the proteoliposomes.

pH titration

pH titration of purified KR2 was essentially performed as described previously (29,34). The pH-dependent UV/Vis absorption spectra were recorded for each pH step for 0.05%-DDM-solubilized KR2 in 100 mM NaCl. The wavelength λ_{max} of the absorption maxima of the retinal bound Schiff base were plotted against the respective pH. A Boltzmann function was fitted to the datasets.

Whole-cell pumping assay

Light-induced ion transport was probed by a whole-cell assay (35) on *E. coli* C43(DE3) cells with overexpressed KR2. Outward transport of protons is directly monitored by the pH decrease of the bacterial suspension. Outward-directed sodium transport results in a pH increase induced by a charge imbalance, which is compensated by proton influx across the *E. coli* cell membranes. After expression, cells were washed several times in sterile, distilled water and transferred into unbuffered pumping solution, containing either 100 mM NaCl or 0 mM NaCl, 10 mM $CaCl_2$, 10 mM $MgCl_2$ to probe the pumping mechanism in the absence of sodium. Additional controls with 100 mM KCl were caried out leading to the same results as with 0 mM NaCl (not shown). Highest reproducibility was achieved when carrying out these experiments directly on fresh cells avoiding freezing and thawing. The OD_{600} was adjusted to 16. A volume of 1 ml of this cell suspension was used for the transport measurements and subjected to the following illumination protocol: dark (1 min) – light (4 min, green light, Schott KL 1500LCD light source) – dark (2 min), during which the pH was constantly measured every 4 s under mild stirring.

Solid-state NMR spectroscopy

MAS-NMR experiments were recorded on either a Bruker Avance III 850 or 900 MHz spectrometer equipped with wide bore Bruker E-free HCN triple resonance or narrow bore HCN triple resonance 3.2 mm probeheads, respectively, at MAS rates of 14 or 16.5 kHz at 275 K. Experiments on NMR samples containing 100 mM NaCl were performed at 265 K in order to compensate for salt-induced heating effects.

All NMR samples were adjusted to a pH 8.5 and doped with 2 mM paramagnetic Gd-DOTA. Amounts of 12 mg of KR2 or 7 mg $KR2_{H180A}$ were loaded into a thin wall or standard 3.2 MAS rotor, respectively. External chemical shift referencing was carried out with respect to DSS through the carboxyl signal of crystalline alanine at 179.85 ppm. Uniformly sampled datasets were Fourier-transformed and processed with a Gaussian apodization (direct dimension) and a QSINE function (indirect dimensions). Non-uniformly sampled datasets were reconstructed by compressed-sensing algorithm within TopSpin 4.1 (Bruker). Analysis of 3D- and 4D experiments was carried out using CCPN (36). All experimental parameters are listed in Tab. S5.

Flash photolysis experiments

Time-resolved measurements were performed via UV/vis flash photolysis. The pump pulses are generated by a Nd:YAG laser, which is coupled to an optical parametric oscillator (OPO). The broadband probe pulses are generated by a Xenon-flashlamp. The pulse sequence is synchronized by a pulse-delay generator, which also controls the detection unit. In order to reduce noise, the spectral edges are cut off with respective filters, resulting in a probing range

of 350-650 nm. Experiments were carried out on KR2 in 0.05% DDM at pH 8.5 with and without 150 mM NaCl at 293 K. Control experiments with N-Methyl-D-glucamine (NMG) at the same ionic strength resulted in an overall similar photocycle dynamics (not shown). All samples were roughly adjusted to a similar OD, to simplify comparability of signal amplitudes.

Results

pH titration and ion pumping of the KR2$_{H180A}$ mutant

The pH dependence of λ_{max} of KR2$_{H180A}$ allows a comparison of its titration characteristics compared to KR2 and KR2$_{H30A}$ (Fig. 1d). The curves are mainly affected by the Schiff base counter ion D116, although other titratable groups such as D251 could contribute as well.

The obtained KR2 titration curve agrees with previous reports (29) and can be described with a pKa of 5.2 ± 0.1. Slightly higher and multiple pKa values have been reported based on the analysis of pH-dependent absorbance changes (1). For KR2$_{H30A}$, the λ_{max} pH titration becomes more sigmoidal reflecting higher cooperativity and specificity in sodium pumping (pKa 5.9 ± 0.1) (29). In contrast, the KR2$_{H180A}$ titration curve is shifted towards lower pH values (pKa < 3.3) and does not show a plateau in the here tested acidic pH range. The observed differences in the titration characteristics of D116 between wild type and both mutants indicate alterations in its H-bonding pattern. While the pKa for KR2$_{H180A}$ is low and similar to that of the primary proton acceptor D85 in bacteriorhodopsin (37), additional interactions must occur in KR2 and KR2$_{H30A}$ to stabilize their higher pKa values. In the here investigated pentameric state (11) and as evaluated by computational studies for the wild type (38), N112 donates an H-bond to S70 which donates an H-bond to D116 stabilizing its ionized state together with four water molecules and an H-bond to the protonated Schiff base. For KR2$_{H30A}$, a slightly shorter distance between Schiff base nitrogen and Cγ of D116 was observed in its X-ray structure (6YC1) (11) together with a deshielding of ^{15}N Schiff base resonance, which could be in line with a stronger H-bond interaction (29). The altered behavior of KR2$_{H180A}$ must then be caused by mutation-induced alterations of interactions partners as discussed further below.

The effect of the H180A mutation on the ion pumping activity of KR2 has been probed using a whole-cell pumping assay (1,35) as shown in Fig. 1e. For KR2, a pH reduction upon illumination is observed in the absence of NaCl, which is caused by outward-directed H^+ pumping. In the presence of 100 mM NaCl, KR2 pumps Na^+ outwards resulting in an electrochemical gradient, which is compensated by an inward movement of H^+ yielding a pH increase (Fig. 1e, left). In contrast, the KR2$_{H30A}$ mutant shows the same effect in the presence of NaCl, but loses its ability of H^+ transfer in the absence of NaCl (1,29) (Fig. 1e, middle). New is our observation that introducing the H180A mutation has a complementary effect to the

H30A mutant: Despite the presence of 100 mM NaCl, no pH change could be observed, which means that no electrochemical gradient is established because the mutant lost the ability of outward Na^+ as well as H^+ pumping (Fig. 1e, right). However, light-induced outward H^+ transfer occurs in the absence of NaCl.

The H180A mutation does not affect the functionally relevant pentameric oligomer as revealed by BN-PAGE analysis in detergent and after reconstitution into DMPC/DMPA lipid bilayers (Fig. S1b).

Resonance Assignment of KR2

In order to understand the reasons for this surprising observation, we performed a full chemical shift resonance assignment of KR2 with the aim of identifying mutation-induced changes. We have applied previously a similar approach for $KR2_{H30A}$, which was however just based on a partial 50% KR2 assignment (29). Here, we report now an almost complete data set, which was obtained by multiple complementary 3- and 4 dimensional heteronuclear spectra acquired at high magnetic fields.

Data acquisition was accelerated by reducing the ^1H T_1 relaxation time through paramagnetic doping of the proteoliposome samples with 2 mM Gd-DOTA (26) and the use of a duty-cycle-optimized MAS probe head with reduced E-field, which enabled 2.5-times faster acquisition (39). Furthermore, the transfer efficiency of the NCA, NCO and CON cross polarization (CP) steps in many of our experiments could be substantially improved by utilizing numerically calculated optimal control (OC) pulses (28), which compensate signal losses caused by radio frequency (RF) field inhomogeneities and modulations in RF phases and amplitudes induced by the MAS sample rotation. Here, signal intensity increased by a factor of 1.65 for NCA and 2.15 for NCO magnetization transfer steps (Fig. 2a). In addition, data were recorded using a non-uniform sampling (NUS) scheme (25,40), which reduces the amount of time domain data points in the indirect dimensions. Here, a NUS-rate of 60% in combination with T_2 weighting (4 ms for ^{15}N and 7 ms for ^{13}C nuclei) was applied and spectra were reconstructed using the compressed sensing algorithm (41). The validity of the method is illustrated by comparison with a uniformly sampled data set (Fig. 2b). If applied together, these methods result in almost 10-times faster data acquisition. Here, 4.5 days were needed for well-resolved 3D NCACX and 9 days for 4D NCOCACB spectra of KR2 (Fig. 2c, Tab. S5).

The resonance assignment of KR2 was carried out in the absence of sodium in order to avoid RF-induced heating effects inside the sample during long 3D and 4D experiments and to evade complications by sodium-induced line broadening. Specific effects caused by the presence of sodium on functionally important sites are explored further below by selective experiments.

Three differently labelled samples were prepared: uniformly labelled KR2 ([U-^{13}C,^{15}N]-KR2), reverse labelled KR2 ([U-^{13}C,^{15}N, rev-FYLIV]-KR2) and forward labelled KR2 ([^{13}C,^{15}N-FYLIV]-KR2). The samples were reconstituted into DMPC/DMPA liposomes. The previously reported partial (50%) assignment was based on 3D NCACX, NCOCX (42), CONCA (43) experiments (29). This dataset has now been completed by additional 3D NCACB, NcoCACB, CANcoCA spectra and using a complementary 4D NCOCACB experiment. A representative assignment walk defining backbone, side chain and neighboring spin systems is shown in Fig. S2. In this way, 203 of 280 residues could be assigned. Furthermore, in INEPT-based experiments, 30 residues could be identified, which do not contribute to the assignable set of residues when using a CP-based experimental schemes. These residues were excluded from further analysis. Our assignment therefore covers 85% of the CP-assignable set of residues. They cover the transmembrane helices and many residues of the extra- and intracellular loops as well as N- and C-terminal regions. The obtained data set now contains most functionally important residues: for example, the key motif N112, D116, Q123 or S64 within the ion uptake and Q78 within the ion release region. Furthermore, retinal chemical shifts and assignment of the protonated Schiff Base were published by our group in our previous study (29). The extent of our assignment is illustrated by highlighting it on the KR2 3D structure in Fig. 3a (see also Fig. S2a) and by mapping it onto a 2D NCA spectrum of [U-^{13}C,^{15}N]-KR2 in Fig. 3b. All chemical shifts are listed in Tab. S1 and are available in the BMRB data base (51639).

Based on these assignments, a secondary structure analysis was performed using secondary chemical shift calculations (44). Positive values indicate alpha helical regions and negative values correspond to deviations, thus beta sheet or loop elements. The predicted secondary structure elements are compared to those found in the monomeric (PDB 6TK6, (12)) and pentameric (PDB 6REW, (7)) KR2 crystal structures (Fig. S3). A very good agreement is found within the limits of such a secondary structure prediction. All seven transmembrane helices and structural details such as the antiparallel β-sheet in the BC loop as well as an α-helical N-terminal cap are reflected by the NMR resonance assignment (Fig. S3).

Effect of NaCl on the assigned residues

To probe the effect of NaCl, proteoliposome samples were washed and incubated in 100 mM NaCl containing NMR buffer. A set of 1D and 2D/3D spectra (^{15}N CP, ^{13}C-^{13}C DARR, ^{15}N-^{13}C NCACX) were recorded in order to analyze effects on functionally important sites.

Most notably, the Schiff base nitrogen resonance broadens and shifts by approx. – 2ppm (Fig. 4a). Similarly, the Nε2 resonance of H30 and H180 also broaden, but only H30 shifts by -2 ppm. In contrast, no substantial salt-induced effect is observed on the retinal ^{13}C chemical shifts (Fig. S4).

A comparison of NCACX spectra of [U-^{13}C, ^{15}N]-KR2 recorded with and without NaCl reveals full or partial signal loss for a number of residues, such as for D116 and S70 located in the retinal SB cavity, T83 at the extracellular sodium binding site, K255 forming the SB linkage and Q244 in the ion release cavity (Fig. 4b). Affected residues are summarized in Tab. S4 and highlighted in the 3D structure in Fig. 4a. The detected signal loss could be caused by specific and non-specific sodium binding and subsequent electrostatic effects resulting in large chemical shift changes and/or line broadening due to increased flexibility or increased structural heterogeneity.

Effect of the H180A mutation on the assigned residues

In order to identify mutation-induced effects in KR2, we first compared 3D NCACX spectra of [U-^{13}C, ^{15}N]-KR2 and [U-^{13}C, ^{15}N]-KR2$_{H180A}$ recorded without sodium. In total, 19 spin systems have been identified as being affected by the mutation (Tab. S2, Fig. S2a). These residues are found in helices B, D, E, F, G and in loops AB, BC, CD, EF and FG. Affected residues of functional relevance are S64, located between ion uptake and SB cavity, S70 in the pSB cavity, Y222 in vicinity of the retinal, and Q78, T83, W82, Q157, R243 and Q244 located within the ion release region. The affected sites are highlighted in yellow Figs. S2a and 5a. On the other hand, chemical shifts of the pSB nitrogen (Fig. 4a, Δ= 0.22 ppm), retinal (Fig. S4) as well as NDQ-motif and residues in the ion uptake cavity seem to be rather unaffected by the mutation (Fig. S5).

In the presence of 100 mM NaCl, thus under a condition, in which KR2 would act in its native sodium pumping mode, similar effects as for the wild type are observed. The signals of the Schiff base nitrogen and of Nε of His30 broaden and shift (Fig. 4a), but the chemical shift difference is smaller compared to the wild type. As in the wild type, there is no effect on the ^{13}C retinal chemical shifts (Fig. S4, Tab. S3) and important residues such as D116, S70, T83, K255 and Q244 show signal losses (Fig. S6). Mutant-specific, NaCl induced chemical shift changes were only observed in case of very few, non-functional residues and therefore seem to be unspecific (Fig. S7). All affected spin systems are listed in Tab. S4.

The above discussed data allow a preliminary interpretation and a first explanation for H180A's changed ion selectivity. The chemical shift analysis reveals, that H180A causes some long-range changes throughout KR2, whereas the chromophore is unaffected. Affected residues of known functional relevance are mainly found in the ion release areas. Consequently, it can be hypothesized, that sodium uptake might take place, but that it is not released to the extracellular side and blocks proton transfer. To clarify this assumption, optical spectroscopy is needed since sodium uptake is linked with the formation of the O-state (45).

Time-resolved optical spectroscopy of $KR2_{H180A}$

Flash photolysis experiments were carried out on KR2 and $KR2_{H180A}$ with and without sodium. The aim of these experiments, besides of a kinetic characterization of the H180A mutant, was to specifically probe whether the mutation affects the formation of the O-state. The O-state has been shown to be associated with the presence of transiently bound sodium within KR2 during the transport cycle (45). Since $KR2_{H180A}$ does not seem to pump sodium, the question arises whether it at least binds inside the protein cavity due to the formation of an O-state.

At first glance, in the presence of salt, the $KR2_{H180A}$ photocycle appears similar to KR2 under identical conditions (Fig. 6a). All major intermediates (K, M and O) are found. However, a closer look into the lifetime distribution map (LDM) of the kinetic data shows that the mutant exhibits an elongated decay of the K-intermediate (and in parallel an elongated rise of M). The M-intermediate then decays in the range of 600 µs to 2 ms in both the mutant and the wild type (with a slightly faster decay in the wild type). In the latter case, this decay just leads to the formation of the O-intermediate. In the mutant, however, one can identify an additional blue-shifted difference signal at around 410 nm (M_2), which is missing in the wild type. The decay of this spectral component occurs at around 10 ms and is slightly delayed in respect to the decay of M_1. This split of the M-intermediate becomes more pronounced in salt-free conditions (Fig. 6b). Here, the photocycles of wild type and $KR2_{H180A}$ look fundamentally different. In the wild type, all photointermediates are generally low populated (in addition to the slower kinetics) and no significant O-state population can be detected. In contrast, KR_{H180A} again shows large difference amplitudes. Most notably is a temporally and spectrally broad M-intermediate. This M-intermediate shows two clearly distinguishable decays, one of which is centered around 450-470 nm (M_1) with a lifetime of approximately 1 ms, and another one centered around 410-420 nm (M_2) with a lifetime of approx. 50 ms. With the decay of the faster component, a red-shifted signature at 630-650 nm (O_1) rises. Surprisingly, a second red-shifted signature at around 570-600 nm (O_2) rises alongside the decay of M_2 at around 50 ms. By the end of the measurement window, the residual amplitude of the ground state bleaching (GSB) and the O_2 state remains (which is reflected in the “infinity” lifetime of the last LDM components).

In the presence of sodium, both the wild type and the $KR2_{H180A}$ show a strongly pronounced O-state, even though sodium transport is not observed in $KR2_{H180A}$ (Fig. 1e). The spectral similarity could still arise from a similar configuration in the retinal binding pocket, which allows a transient binding of sodium but somehow prohibits a vectorial transport. The key difference lies in the additional M_2 component in $KR2_{H180A}$, which is completely missing in the wild type. The elongation of the M-state in the form of an equilibrium between M_1 and M_2 in the mutant implies a delay of the reprotonation step at the Schiff base (or conversely the deprotonation of the counterion), which normally is crucial to prevent a backflow of the sodium ion. At the same

time, proton transport might also be prevented (Fig. 1e) due to the presence of the loosely coordinated sodium ions, which themselves have a major electrostatic effect in the direct vicinity of the retinal binding pocket.

In the absence of sodium, the split into M_1 and M_2 in $KR2_{H180A}$ is even more pronounced. Interestingly, $KR2_{H180A}$ does not just show an O-like signature despite the missing sodium ions, but it even splits into two spectrally distinguishable components (O_1 and O_2). The presence of two O-substates has been discussed for the KR2 wild type and other sodium pumps as well (14,15,38), however in those cases the signatures were not as clearly separated as in $KR2_{H180A}$. In essence, the transition from O_1 to O_2 was ascribed to the reisomerization step from *13-cis* to *all-trans* retinal. This could also be rationalized by considering the signature in the near-UV (SBS), which was proposed to be a marker band for the 13-*cis* configuration of the chromophore in KR2 (16), and which clearly decays alongside the O_1-intermediate (Fig. 6b). Consequently, one could argue that O_1 contains the 13-*cis* and O_2 the *all-trans* chromophore.It has also been argued that previous X-ray and NMR data on the O-state (11,21) would then correspond to O2 while published X-FEL data (12) would then refer to O1 (14).

Discussion

Understanding and manipulating the ion selectivity of the light-driven sodium pump KR2 is the key for turning it into a potential optogenetic tool. Therefore, rationalizing the effect of site-directed mutations on KR2's transport activity by elucidating their structural and photodynamic consequences will help to better understand ion transport and to identify key factors by which it can be altered. A number of mutations which effect ion pumping have been demonstrated for KR2 of which especially H30A attracted interest as it suppresses the proton pumping mode in the absence of NaCl but retains the sodium pumping functionality (Fig. 1e, middle). H30 has also raised interest as it is located at the oligomerisation interface within the KR2 pentamer and in other microbial rhodopsin ion pumps, such Histidines have been found to be functionally important (46-48). Here, we report that the H180A mutation of the second Histidine has a complementary functional effect as it suppresses sodium pumping while retaining proton pumping in the absence of sodium. The structural reasons are not immediately obvious as H180 is located in helix E pointing away from the pentamer and is not part of the ion selectivity, capture or release clusters (Fig. 1a). However, the H180A mutation has long-range effects on multiple residues (Fig. 5a) with some of them located along the ion translocation pathway. Interestingly, it is not affecting the chromophore, Schiff base nitrogen, and the NDQ motif.

Inspecting the KR2 3D structure 3REW reveals, that H180 is surrounded by residues V184, I181, F177 in Helix E and Q141, F142 and S145 in Helix D (Fig. 7a). Unfortunately, only three of them could be assigned (highlighted in green in Fig, 7b) and only I181 shows a strong

spectral response upon mutation. It is however reasonable to assume, that the H180A mutation disturbs the interaction network between these residues across helices E and D, which then triggers further structural changes throughout the protein by altered helix-helix couplings.

For example, residues Y154 and Q157 at the extracellular end of helix D are affected and perturbations are further propagated towards residues at the extracellular sides of helices B (Q78, W82, T83), F (Y222) and G (R243, Q244). Interestingly, the site around H180 also responds to sodium (Fig. 7b), indicating that KR2 is able to sense the presence of ions via multiple sites.

However, sodium sensing is not abolished by the H180A mutation as the pattern of sodium-dependent spectral changes is almost identical between KR2 and $KR2_{H180A}$ (Fig. 4, Tab. S4). Furthermore, an O-state clearly forms also in the mutant. The formation of such an intermediate is linked with transient sodium binding during the photocycle, which therefore seems to takes place, although no net-transport by $KR2_{H180A}$ is detected. This observation is compatible with the absence of spectral changes of residues involved in the transient binding such as N112, D116 and the Schiff base nitrogen.

In contrast, a strong spectral response was observed for residues along the putative translocation pathway (Fig. 7c) such as S64, S70, Q78, W82, T83, Q244 and R243: Residue S64, together with Q123, controls entry and ion backflow between the intracellular side and the ion pathway. S70 also plays a role in preventing backflow and is part of the H-bond network stabilizing D116 in the ground state. Q78 is part of the ion release pathway suggested by Kovalev et al. (11) and W82, T83 and Q244 are found in close proximity. In addition, R243 is part of a negatively charged cluster with E11 and E160, which was also suggested to be involved in ion release (1,5,6) or protein stability (11).

A possible explanation for the loss of sodium pumping by $KR2_{H180A}$ could be that sodium is taken up, enters the transient binding site, but the release along Q78 or R243 is blocked. Instead, ion backflow takes place, which is usually prevented by S64-Q123 (11). The transient sodium binding is in line with the observed O-state formation in $KR2_{H180A}$ in our flash photolysis data (Fig. 6a). Furthermore, the observed delay of the Schiff base reprotonation during the photocycle agrees with a loss of backflow control. The lack of proton pumping activity in the presence of sodium is then caused by electrostatic effects due to bound sodium within KR2 during the photocycle.

Previous studies on microbial rhodopsins revealed a functional importance of Histidines located at the pentamer interface (H75 in PR, H30 in KR2) (29,46). In PR, a proton pump, H75 seem to act as a potential pH regulator. It forms a triad across the oligomerization interface connecting the primary proton acceptor D97 of one protomer with W34 of the adjacent protomer. It was found that this interaction, which depends on the charge state of His with a

pKa close to the environmental pH, is modulated during the photocycle as His75 switches from τ to π and changes its ring orientation in the M-state.

In KR2, also H30 seems to mediate long-range interactions across the oligomerisation interface (29,31), while mutating H180 indicates primarily a role within its own protomer. Whether these residues alter their tautomeric and rotameric states during the photocycle as in PR cannot be concluded from our data and would need further investigations by DNP-enhanced ssNMR on cryo-trapped photointermediates. A comparison of the pentameric O-state X-ray structure (6XYT) (11) with the corresponding dark state shows identical orientation of the H180 sidechain but variations for H30, while the XFEL data (6TK2, 6TK6) (12) indicate a displacement of H180 but identical orientation of H30.

The extensive resonance assignment of KR2 also allows to probe the presence of sodium. A recent Raman study has shown an allosteric communication between the retinal chromophore upon ion binding (49). A shifted v(C=N) signal was interpreted as a weakened H-bonding network of the Schiff base and the lack of changes of the HOOP band indicated that no significant distortion of the retinal took place. The authors suggested that the sodium bound to the external binding site at the protomer interface is important for stabilizing the oligomer. Here, as illustrated in Fig. 4a and summarized in Tab. S4, many sites within KR2 show a spectral response even within the core of the protein. As these data were recorded on dark state KR2, the internal, transient binding site is not present and the observed effects represent long-range effects from external sodium binding. Especially noteworthy is the shift and broadening of the ^{15}N chemical shift of the Schiff base nitrogen by about -2 ppm indicating a weaker H-bonding network. This observation is in line with the trend reported by others (31). Interestingly, the ^{13}C chemical shifts of the retinal carbons do not change (Fig. S4). The effect on Schiff base and retinal has been reproduced by automatic fragmentation QM/MM simulations (50). Also, residues within the binding pocket such as Y217 and W113 close to the polyene chain, Y222 close to the ring or the counter ion D116 show strong effects in the presence of sodium. Overall, similar effects were observed for both KR2 and KR2$_{H180A}$. Our data indicate that the presence of sodium bound in the external binding site and its electrostatic effects when bound to the membrane and to the protein surface, could prepare the protein for subsequent sodium binding steps upon illumination.

Conclusions

Multidimensional solid-state NMR spectroscopy has been used to probe site-resolved allosteric effects effects of sodium binding and of the H180A mutation on KR2 in its ground state. The H180A mutation triggers long-range effects within the ion release pathway with surprising functional consequences. Our data suggest that the loss of sodium- and proton

pumping in the presence of sodium is caused by transient sodium binding while vectorial transport is prevented. For this mutant, sodium seems to act as a strong silencer for proton pumping. Furthermore, our data show that the presence of sodium is sensed by KR2 througout the protein and affects even the Schiff base nitrogen. Such long-range electrostatic effects could provide a mechanism to prepare the protein for subsequent ion uptake steps upon illumination. On the technical site we can conclude that the combination of methods for accelerated NMR data acquisition (NUS, Gd-doping, optimal control pulse sequences) applied here to a challenging system holds great potential for future applications.

Acknowledgments

This paper is dedicated to Klaus Gawrisch. His great work on the biophysics of lipids and membrane proteins had an important impact on our research. CG thanks Klaus for many friendly and insightful discussions. This work was funded by DFG/SFB807 “Transport and communications across membranes” and DFG grant 391643887. Jinhuan Zhang and Xiao He, New York University & East China Normal University Shanghai, are acknowledged for helpful discussions and sharing computational data. Jakob Maciejko, Lea Becker and Orawan Jakdetchai are acknowledged for support and discussions. We thank Richard C. D. Brown, Southampton for his continuous support with retinal synthesis.

Author Contributions

CNK carried out all the NMR experiments, analyzed data, prepared samples, prepared figures and wrote the paper. MA contributed data on time-resolved optical spectroscopy, prepared figures and contributed to data interpretation, discussion and paper writing. JK provided functional data and protocols, helped with sample preparation and biochemical characterization. JO carried out mutations and functional analysis. PB helped with NMR experiments, functional analysis and data analysis. JBB helped with the NMR experiments, project design and data analysis. JW contributed to data interpretation and discussion. CG designed the project, contributed to data analysis and interpretation, prepared figures, wrote the paper.

Declaration of Interests

The authors declare that they have no competing interests that could have appeared to influence the work reported in this paper.

Figures and Legends

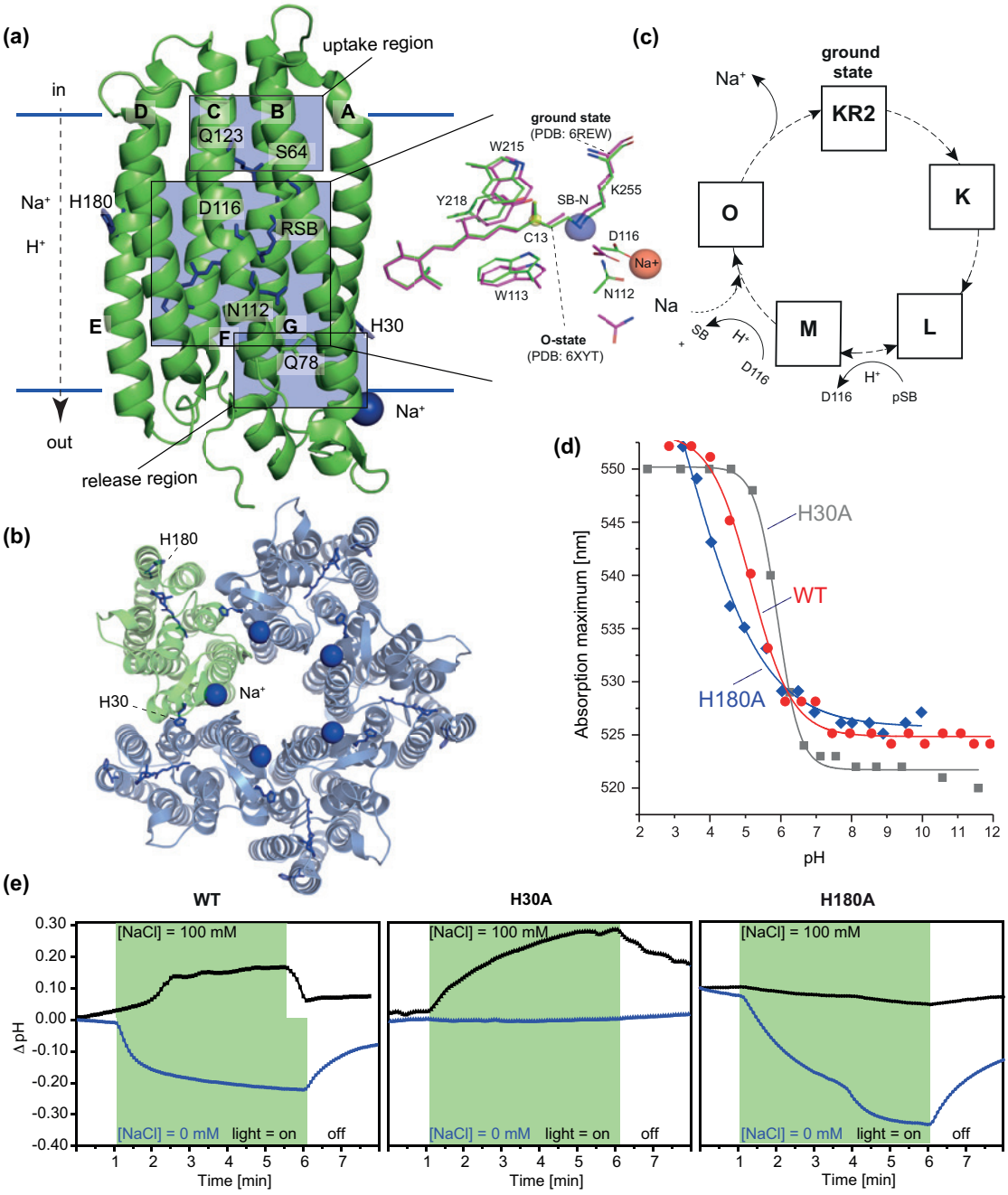

Figure 1: KR2 structure and function. (a, b) Pentameric KR2 structure (PDB 6REW (7)). The NDQ motif, ion uptake and release regions as well as residues His30 and 180 and the external Na^+ binding site are highlighted. The inset shows the transient Na^+ binding site which occurs during the transport cycle in the O-state (PDB 6XYT, (11)). Transient Na^+ binding causes a red shift and a de-shielding of the Schiff base nitrogen and retinal carbon C13 (21), as indicated by colored spheres. **(c)** KR2 photocycle: The O-state is linked to Na^+ transport (5). **(d)** pH dependence of λ_{max} of KR2, $KR2_{H30A}$ and KR_{H180A} (0.05% DDM, 100 mM NaCl). The curve for $KR2_{H30A}$ is more sigmoidal compared to the wild type, while the H180A mutation causes a lowering of the pKa of the Schiff base counter ion D116 (pKa of KR2, $KR2_{H30A}$, KR_{H180A} = 5.2 ± 0.1, 5.9 ± 0.1, ≤ 3.3, respectively). The $KR2_{H30A}$ curve has been replotted from (29). See Fig. S1a for full spectra of KR2 and $KR2_{H180A}$. **(e)** Whole-cell pumping assay. Without NaCl, KR2 pumps H^+ outside resulting in a pH drop (left). In presence of NaCl, KR2 pumps

Na^+ outside resulting in an electrochemical gradient, which is compensated by inward movement of H^+ yielding a pH increase (left). In $KR2_{H30A}$ mutation, the sole H^+ pumping ability is abolished (middle) as shown before (1). For $KR2_{H180A}$, in presence of NaCl, no Na^+ nor H+ transfer is observed, while in the absence of NaCl, H^+ pumping occurs as for the wild type (right).

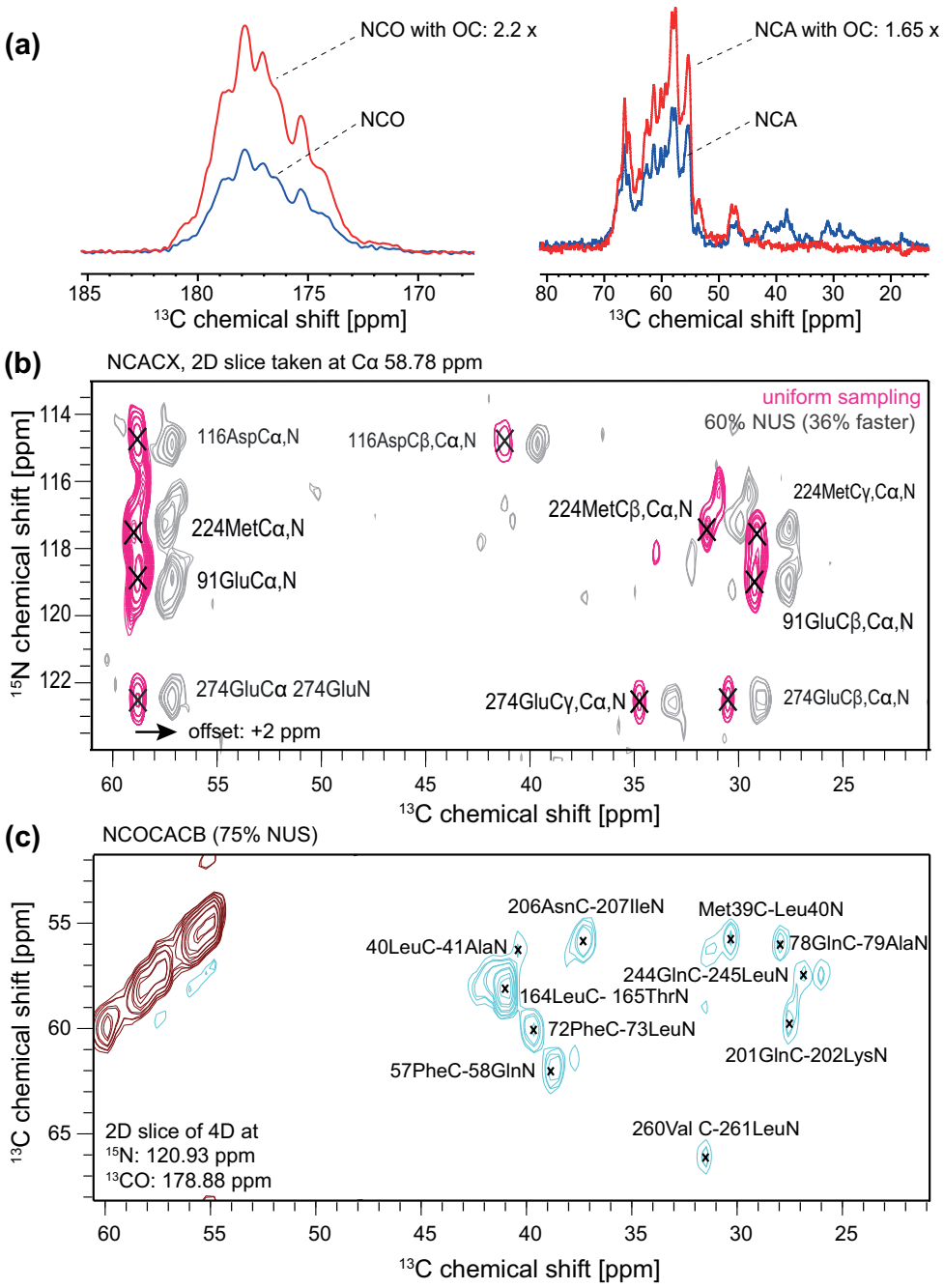

Figure 2: Methods for optimized data acquisition. (a) Comparison between 1D NCO (left) and NCA (right) spectra of [U-^{13}C,^{15}N]-KR2 recorded using 'conventional' spin-lock pulses for cross polarization or pulses calculated based on optimal control theory (28) (900 MHz, 20 kHz MAS). **(b)** Comparison between uniform (pink) and non-uniform (blue) sampling schemes. Shown is a 2D slice from a 3D NCACX spectrum of [U-^{13}C,^{15}N, rev-FYLIV]-KR2 (850 MHz, 14 kHz MAS). A sampling rate of 65% together with T2 weighting has been applied. The spectrum

was reconstructed using Compressed Sensing (25). **(c)** 2D slice from a 4D NCOCACB spectrum of [U-^{13}C,^{15}N]-KR2 (900 MHz, 14 kHz MAS, 75% NUS). The total acquisition time of the full 4D spectrum was 9 days. All experimental parameters are summarized in Tab. S5.

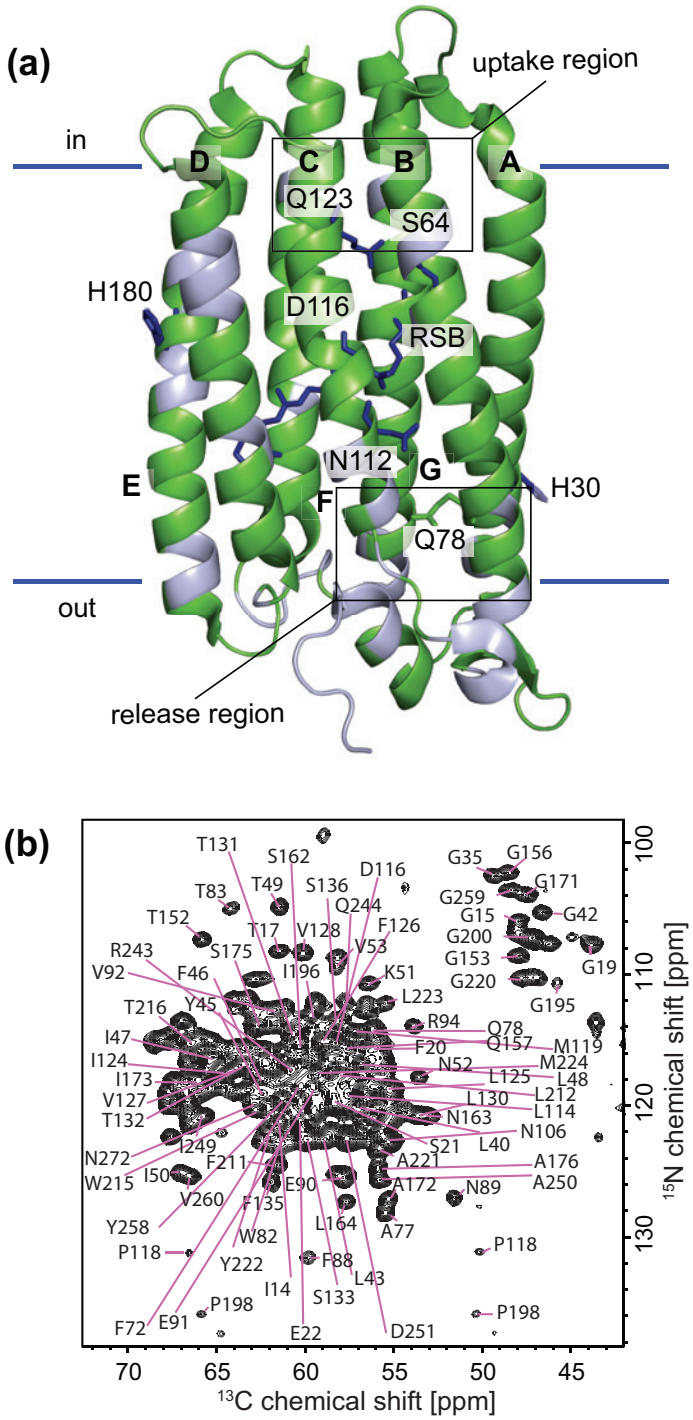

Figure 3: Chemical shift assignment of KR2. (a) The resonance assignment covers more than 80% of all sequentially assignable residues (203) including sidechains. Assigned residues are shown in green in the pentameric X-ray structure of KR2 (6REW (7), only one protomer shown. See also Fig. S2 for an assignment walk and Fig. S3 for a secondary chemical shift analysis. The assignment is summarized in Tab. S1. **(b)** Projection of the backbone assignment onto a 2D NCA spectrum of [U-^{13}C,^{15}N]-KR2. Experimental details are provided in Tab. S5.

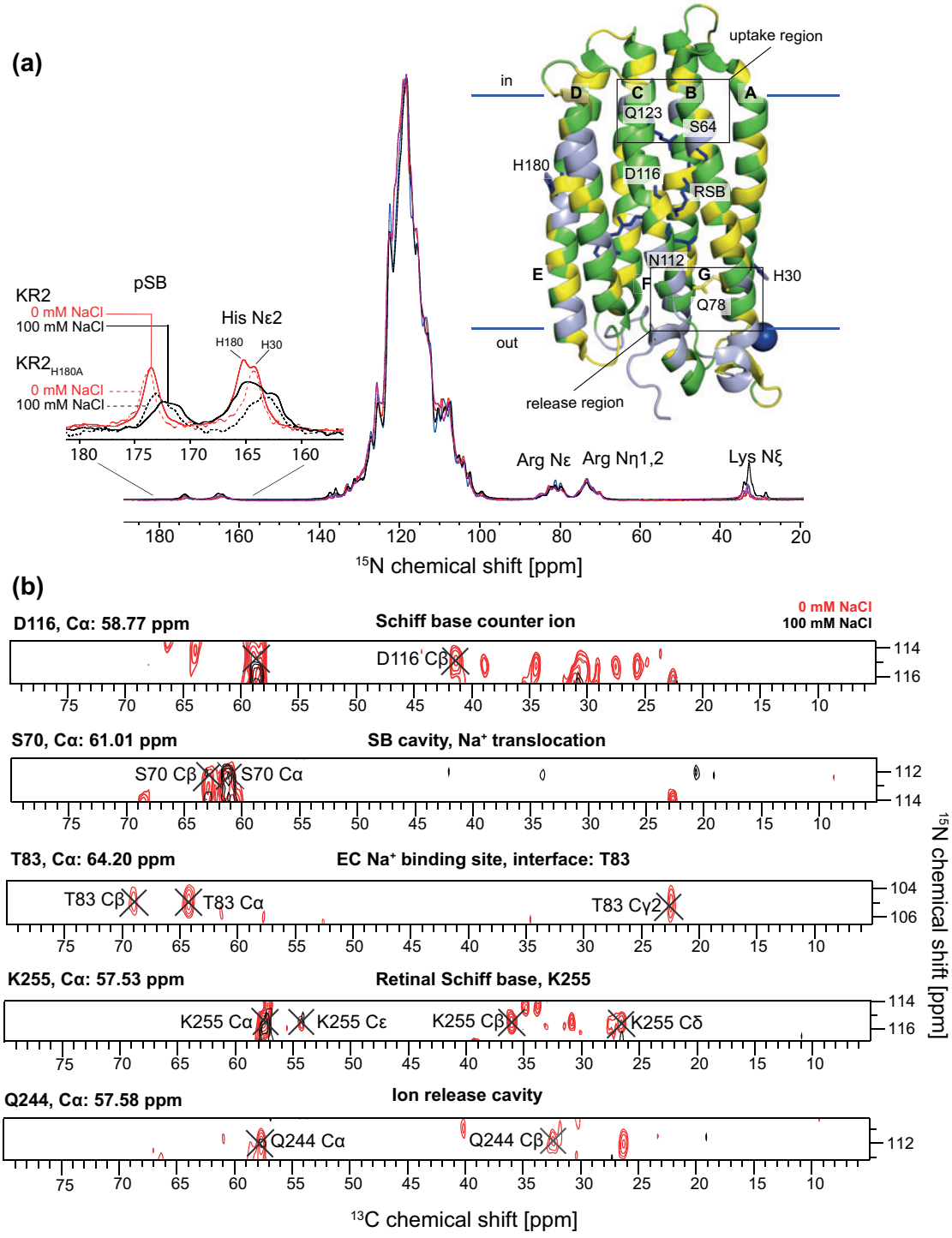

Figure 4: The effect of sodium on ^{13}C- and ^{15}N spectra of KR2. (a) ^{15}N CP-MAS NMR spectrum of [U-^{13}C, ^{15}N]-KR2 recorded without (red) and with 100 mM NaCl (black). The pSB, H30 and H180 signals broaden and shift in the presence of sodium. A similar effect is observed for $KR2_{H180A}$ (red/black dotted lines). The inset shows the KR2 structure as in Fig. 3 but with affected residues colored in yellow. **(b)** Selected slices from 3D NCACX spectra of [U-^{13}C, ^{15}N]-KR2 recorded without (red) and with 100 mM NaCl (black). Spin systems were selected, which show broadening / peak reduction upon addition of sodium (see Tab. S4). The sodium-induced effects are shown in yellow in the X-ray structure of KR2 (6REW). Experimental details are provided in Tab. S5.

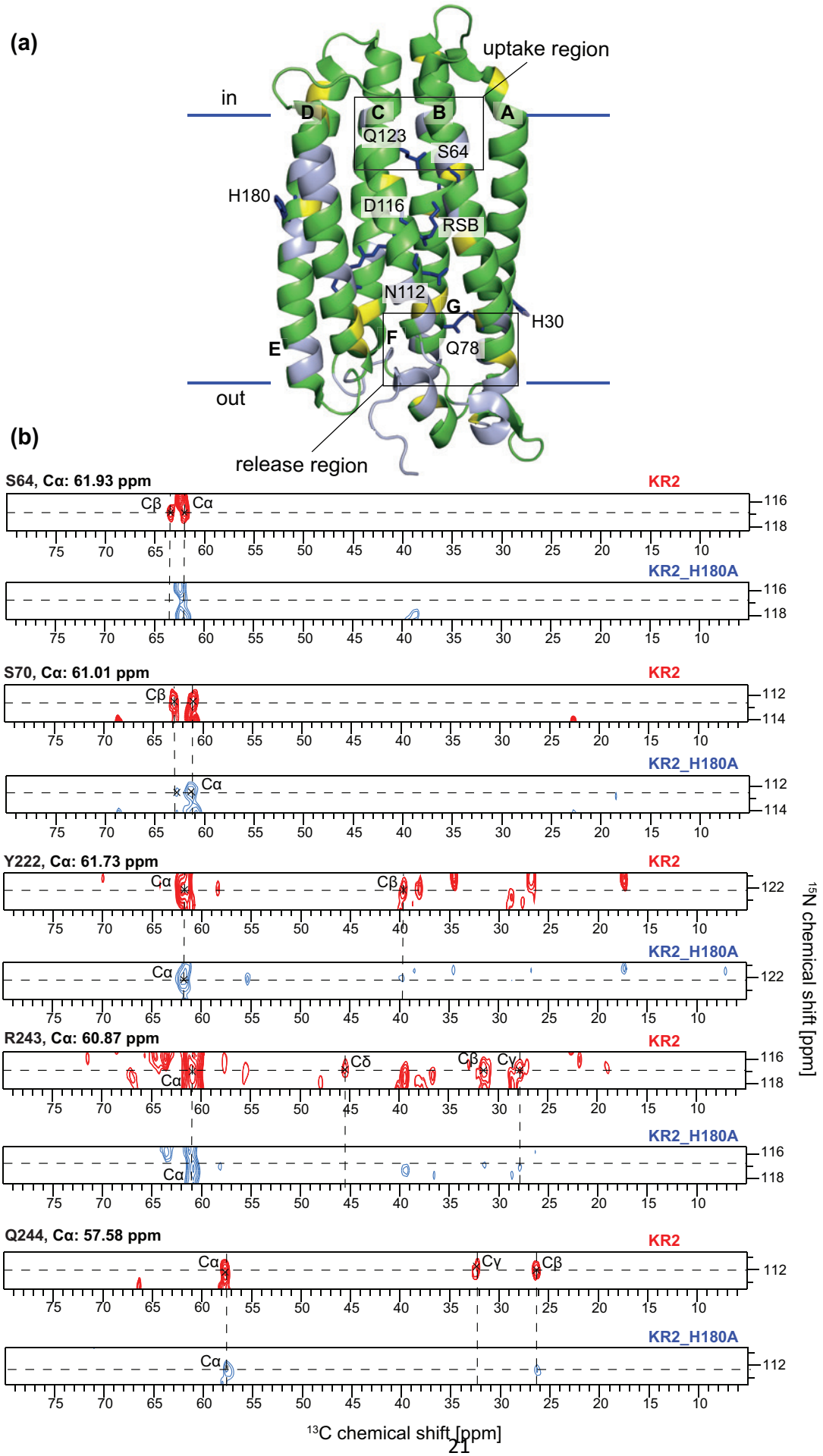
(a)
uptake region
in
D
C
B
A
Q123
S64
H180
D116
RSB
N112
G
H30
E
F
Q78
out
release region
(b)
S64, Cα: 61.93 ppm
KR2
Cβ
Cα
KR2_H180A
S70, Cα: 61.01 ppm
KR2
Cβ
KR2_H180A
Cα
Y222, Cα: 61.73 ppm
KR2
Cα
Cβ
KR2_H180A
Cα
R243, Cα: 60.87 ppm
KR2
Cα
Cδ
Cβ
Cγ
KR2_H180A
Cα
Q244, Cα: 57.58 ppm
KR2
Cα
Cγ
Cβ
KR2_H180A
Cα
15N chemical shift [ppm]
13C chemical shift [ppm]

Figure 5: The effect of the H180A mutation on selected KR2 residues. (a) Residues affected by the H180A mutation colored in yellow. Altogether, 19 residues in helices B, D, E, F, G and in loops AB, BC, CD, DE, EF and FG are found. **(b)** Comparison of 2D slices of 3D NCACX spectra of KR2 with $KR2_{H180A}$. Here, only spin systems of functionally relevant residues are shown, which are affected by the mutation (see also Fig. S5). A general summary is provided in Tab. S2 and Fig. S2a. The slices for S64, S70 and Q244 were taken from NCACX spectra of [U-^{13}C,^{15}N, rev-FYLIV]-KR2 / $KR2_{H180A}$.The slices for Y222 and R243 were taken from NCACX spectra of [U-^{13}C, ^{15}N]-KR2 / $KR2_{H180A}$. Experimental details are provided in Tab. S5.

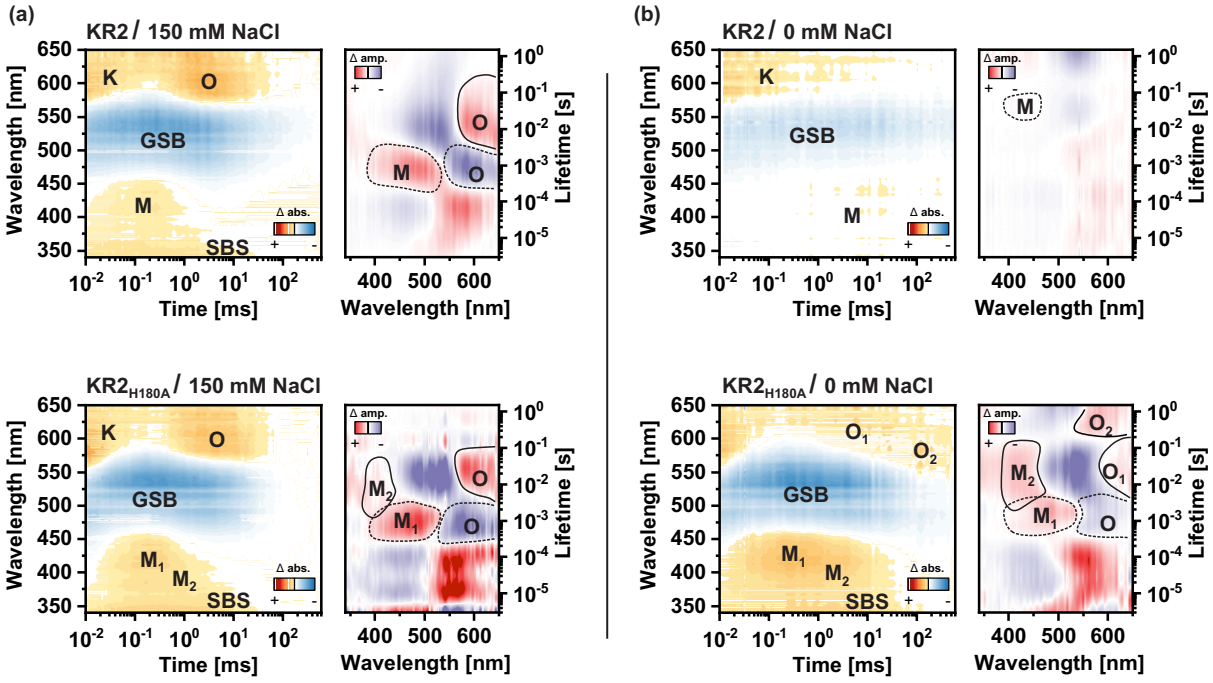

Figure 6: The effect of the H180A mutation on the photodynamics of KR2. (a) Flash photolysis of KR2 and $KR2_{H180A}$ in presence of 150 mM NaCl and **(b)** Flash photolysis of KR2 and $KR2_{H180A}$ in the absence of NaCl. The lifetime components are represented in the lifetime distribution maps (LDMs), which allow a quasi model-free analysis of the kinetic dataset. The corresponding lifetime distributions of the M/M_1-decay / O-rise are marked by the dashed lines. The lifetime of the M_2-decay and the O-decay are marked by the solid lines. An additional component, originating from the O_2-decay is found for $KR2_{H180A}$ in the presence of NaCl.

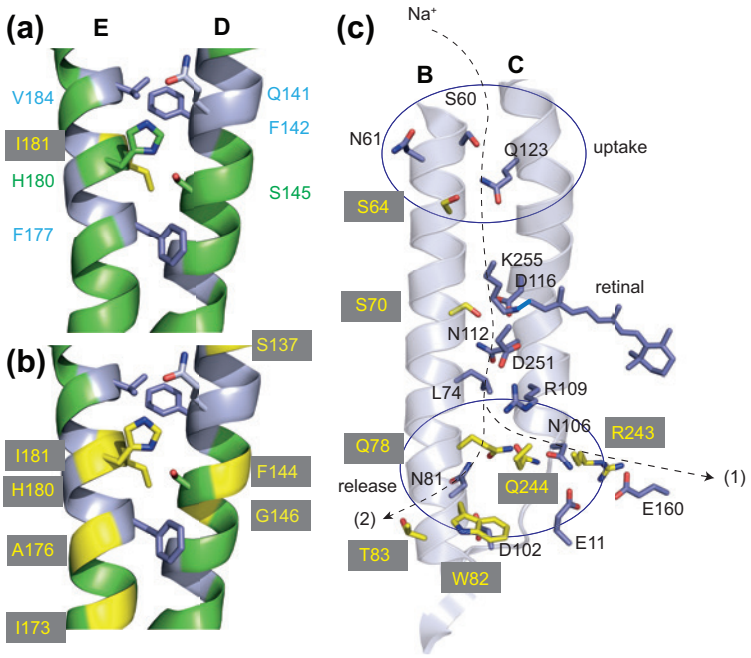

Figure 7: Long-range disturbance of sodium transfer by the H180A mutation. (a) H180 in transmembrane helix E points towards the membrane interface and transmembrane helix D and is surrounded by sidechains of adjacent residues (green: assigned, light-blue: not assigned). A H180A mutation-induced effect is only observed for the assigned residue I181 (yellow). **(b)** The presence of sodium causes spectral changes of assigned residues in this region (yellow). **(c)** Mutation-induced effects on the ion-uptake and release regions. The putative ion transfer pathways are indicated. Affected residues are highlighted in yellow. The mutation seems to enable transient sodium binding during the O-state but release (Q78, R243) and the prevention of backflow (S64, S70) seem to be disturbed. Cartoons were created based on the pentameric KR2 X-ray structure 6REW (7). Fig. (c) was inspired by (11).

Supporting Citations

References (21,29,51-53) appear in the Supporting material.

References

1. Inoue, K., H. Ono, R. Abe-Yoshizumi, S. Yoshizawa, H. Ito, K. Kogure, and H. Kandori. 2013. A light-driven sodium ion pump in marine bacteria. *Nat Commun*. 4:1678, doi: 10.1038/ncomms2689.
2. Otto, H., T. Marti, M. Holz, T. Mogi, M. Lindau, H. G. Khorana, and M. P. Heyn. 1989. Aspartic Acid-96 Is the Internal Proton Donor in the Reprotonation of the Schiff-Base of Bacteriorhodopsin. *Proc Natl Acad Sci U S A*. 86(23):9228-9232, doi: DOI 10.1073/pnas.86.23.9228.
3. Braiman, M. S., T. Mogi, T. Marti, L. J. Stern, H. G. Khorana, and K. J. Rothschild. 1988. Vibrational spectroscopy of bacteriorhodopsin mutants: light-driven proton transport involves protonation changes of aspartic acid residues 85, 96, and 212. *Biochemistry*. 27(23):8516-8520, doi: 10.1021/bi00423a002.
4. Dioumaev, A. K., J. M. Wang, Z. Balint, G. Varo, and J. K. Lanyi. 2003. Proton transport by proteorhodopsin requires that the retinal Schiff base counterion Asp-97 be anionic. *Biochemistry*. 42(21):6582-6587, doi: 10.1021/bi034253r.

5. Kato, H. E., K. Inoue, R. Abe-Yoshizumi, Y. Kato, H. Ono, M. Konno, S. Hososhima, T. Ishizuka, M. R. Hoque, H. Kunitomo, J. Ito, S. Yoshizawa, K. Yamashita, M. Takemoto, T. Nishizawa, R. Taniguchi, K. Kogure, A. D. Maturana, Y. Iino, H. Yawo, R. Ishitani, H. Kandori, and O. Nureki. 2015. Structural basis for Na(+) transport mechanism by a light-driven Na(+) pump. *Nature*. 521(7550):48-53, doi: 10.1038/nature14322.
6. Gushchin, I., V. Shevchenko, V. Polovinkin, K. Kovalev, A. Alekseev, E. Round, V. Borshchevskiy, T. Balandin, A. Popov, T. Gensch, C. Fahlke, C. Bamann, D. Willbold, G. Buldt, E. Bamberg, and V. Gordeliy. 2015. Crystal structure of a light-driven sodium pump. *Nat Struct Mol Biol*. 22(5):390-395, doi: 10.1038/nsmb.3002.
7. Kovalev, K., V. Polovinkin, I. Gushchin, A. Alekseev, V. Shevchenko, V. Borshchevskiy, R. Astashkin, T. Balandin, D. Bratanov, S. Vaganova, A. Popov, V. Chupin, G. Buldt, E. Bamberg, and V. Gordeliy. 2019. Structure and mechanisms of sodium-pumping KR2 rhodopsin. *Sci Adv*. 5(4):eaav2671, doi: 10.1126/sciadv.aav2671.'PMICD:' PMC6457933.
8. Gushchin, I., V. Shevchenko, V. Polovinkin, V. Borshchevskiy, P. Buslaev, E. Bamberg, and V. Gordeliy. 2016. Structure of the light-driven sodium pump KR2 and its implications for optogenetics. *FEBS J*. 283(7):1232-1238, doi: 10.1111/febs.13585.
9. Hontani, Y., K. Inoue, M. Kloz, Y. Kato, H. Kandori, and J. T. Kennis. 2016. The photochemistry of sodium ion pump rhodopsin observed by watermarked femto- to submillisecond stimulated Raman spectroscopy. *Phys Chem Chem Phys*. 18(35):24729-24736, doi: 10.1039/c6cp05240a.
10. Asido, M., P. Eberhardt, C. N. Kriebel, M. Braun, C. Glaubitz, and J. Wachtveitl. 2019. Time-resolved IR spectroscopy reveals mechanistic details of ion transport in the sodium pump Krokinobacter eikastus rhodopsin 2. *Phys Chem Chem Phys*. 21(8):4461-4471, doi: 10.1039/c8cp07418f.
11. Kovalev, K., R. Astashkin, I. Gushchin, P. Orekhov, D. Volkov, E. Zinovev, E. Marin, M. Rulev, A. Alekseev, A. Royant, P. Carpentier, S. Vaganova, D. Zabelskii, C. Baeken, I. Sergeev, T. Balandin, G. Bourenkov, X. Carpena, R. Boer, N. Maliar, V. Borshchevskiy, G. Buldt, E. Bamberg, and V. Gordeliy. 2020. Molecular mechanism of light-driven sodium pumping. *Nat Commun*. 11(1):2137, doi: 10.1038/s41467-020-16032-y.'PMICD:' PMC7195465.
12. Skopintsev, P., D. Ehrenberg, T. Weinert, D. James, R. K. Kar, P. J. M. Johnson, D. Ozerov, A. Furrer, I. Martiel, F. Dworkowski, K. Nass, G. Knopp, C. Cirelli, C. Arrell, D. Gashi, S. Mous, M. Wranik, T. Gruhl, D. Kekilli, S. Brunle, X. Deupi, G. F. X. Schertler, R. M. Benoit, V. Panneels, P. Nogly, I. Schapiro, C. Milne, J. Heberle, and J. Standfuss. 2020. Femtosecond-to-millisecond structural changes in a light-driven sodium pump. *Nature*. 583(7815):314-318, doi: 10.1038/s41586-020-2307-8.
13. Balashov, S. P., E. S. Imasheva, A. K. Dioumaev, J. M. Wang, K. H. Jung, and J. K. Lanyi. 2014. Light-driven Na(+) pump from Gillisia limnaea: a high-affinity Na(+) binding site is formed transiently in the photocycle. *Biochemistry*. 53(48):7549-7561, doi: 10.1021/bi501064n.'PMICD:' PMC4263435.
14. Fujisawa, T., K. Kinoue, R. Seike, T. Kikukawa, and M. Unno. 2022. Reisomerization of retinal represents a molecular switch mediating Na(+) uptake and release by a bacterial sodium-pumping rhodopsin. *Journal of Biological Chemistry*. 298(9):102366, doi: 10.1016/j.jbc.2022.102366.'PMICD:' PMC9483557.
15. Kato, T., T. Tsukamoto, M. Demura, and T. Kikukawa. 2021. Real-time identification of two substrate-binding intermediates for the light-driven sodium pump rhodopsin. *Journal of Biological Chemistry*. 296:100792, doi: 10.1016/j.jbc.2021.100792.'PMICD:' PMC8219890.
16. Asido, M., R. K. Kar, C. N. Kriebel, M. Braun, C. Glaubitz, I. Schapiro, and J. Wachtveitl. 2021. Transient Near-UV Absorption of the Light-Driven Sodium Pump Krokinobacter eikastus Rhodopsin 2: A Spectroscopic Marker for Retinal Configuration. *J Phys Chem Lett*. 12(27):6284-6291, doi: 10.1021/acs.jpclett.1c01436.
17. Kato, Y., K. Inoue, and H. Kandori. 2015. Kinetic Analysis of H(+)-Na(+) Selectivity in a Light-Driven Na(+)-Pumping Rhodopsin. *J Phys Chem Lett*. 6(24):5111-5115, doi: 10.1021/acs.jpclett.5b02371.

18. Chen, H. F., K. Inoue, H. Ono, R. Abe-Yoshizumi, A. Wada, and H. Kandori. 2018. Time-resolved FTIR study of light-driven sodium pump rhodopsins. *Phys Chem Chem Phys*. 20(26):17694-17704, doi: 10.1039/c8cp02599a.
19. Tahara, S., S. Takeuchi, R. Abe-Yoshizumi, K. Inoue, H. Ohtani, H. Kandori, and T. Tahara. 2018. Origin of the Reactive and Nonreactive Excited States in the Primary Reaction of Rhodopsins: pH Dependence of Femtosecond Absorption of Light-Driven Sodium Ion Pump Rhodopsin KR2. *J Phys Chem B*. 122(18):4784-4792, doi: 10.1021/acs.jpcb.8b01934.
20. Kriebel, C. N., J. Becker-Baldus, and C. Glaubitz. 2022. Solid-State NMR Spectroscopy on Microbial Rhodopsins. *Methods Mol Biol*. 2501:181-206, doi: 10.1007/978-1-0716-2329-9_9.
21. Jakdetchai, O., P. Eberhardt, M. Asido, J. Kaur, C. N. Kriebel, J. Mao, A. J. Leeder, L. J. Brown, R. C. D. Brown, J. Becker-Baldus, C. Bamann, J. Wachtveitl, and C. Glaubitz. 2021. Probing the photointermediates of light-driven sodium ion pump KR2 by DNP-enhanced solid-state NMR. *Sci Adv*. 7(11), doi: 10.1126/sciadv.abf4213.'PMICD:' PMC7954446.
22. Becker-Baldus, J., C. Bamann, K. Saxena, H. Gustmann, L. J. Brown, R. C. Brown, C. Reiter, E. Bamberg, J. Wachtveitl, H. Schwalbe, and C. Glaubitz. 2015. Enlightening the photoactive site of channelrhodopsin-2 by DNP-enhanced solid-state NMR spectroscopy. *Proc Natl Acad Sci U S A*. 112(32):9896-9901, doi: 10.1073/pnas.1507713112.'PMICD:' PMC4538646.
23. Bajaj, V. S., M. L. Mak-Jurkauskas, M. Belenky, J. Herzfeld, and R. G. Griffin. 2009. Functional and shunt states of bacteriorhodopsin resolved by 250 GHz dynamic nuclear polarization-enhanced solid-state NMR. *Proc Natl Acad Sci U S A*. 106(23):9244-9249, doi: 10.1073/pnas.0900908106.'PMICD:' PMC2695048.
24. Burakova, E., S. K. Vasa, A. Klein, and R. Linser. 2020. Non-uniform sampling in quantitative assessment of heterogeneous solid-state NMR line shapes. *J Biomol NMR*. 74(1):71-82, doi: 10.1007/s10858-019-00291-z.
25. Lin, E. C., and S. J. Opella. 2013. Sampling scheme and compressed sensing applied to solid-state NMR spectroscopy. *J Magn Reson*. 237:40-48, doi: 10.1016/j.jmr.2013.09.013.'PMICD:' PMC3851314.
26. Ullrich, S. J., S. Holper, and C. Glaubitz. 2014. Paramagnetic doping of a 7TM membrane protein in lipid bilayers by Gd(3)(+)-complexes for solid-state NMR spectroscopy. *J Biomol NMR*. 58(1):27-35, doi: 10.1007/s10858-013-9800-4.
27. Ganapathy, S., A. Naito, and C. A. Mcdowell. 1981. Paramagnetic Doping as an Aid in Obtaining High-Resolution C-13 Nmr-Spectra of Biomolecules in the Solid-State. *J Am Chem Soc*. 103(20):6011-6015, doi: DOI 10.1021/ja00410a003.
28. Tosner, Z., R. Sarkar, J. Becker-Baldus, C. Glaubitz, S. Wegner, F. Engelke, S. J. Glaser, and B. Reif. 2018. Overcoming Volume Selectivity of Dipolar Recoupling in Biological Solid-State NMR Spectroscopy. *Angew Chem Int Ed Engl*. 57(44):14514-14518, doi: 10.1002/anie.201805002.
29. Kaur, J., C. N. Kriebel, P. Eberhardt, O. Jakdetchai, A. J. Leeder, I. Weber, L. J. Brown, R. C. D. Brown, J. Becker-Baldus, C. Bamann, J. Wachtveitl, and C. Glaubitz. 2019. Solid-state NMR analysis of the sodium pump Krokinobacter rhodopsin 2 and its H30A mutant. *J Struct Biol*. 206(1):55-65, doi: 10.1016/j.jsb.2018.06.001.
30. Shigeta, A., S. Ito, K. Inoue, T. Okitsu, A. Wada, H. Kandori, and I. Kawamura. 2017. Solid-State Nuclear Magnetic Resonance Structural Study of the Retinal-Binding Pocket in Sodium Ion Pump Rhodopsin. *Biochemistry*. 56(4):543-550, doi: 10.1021/acs.biochem.6b00999.
31. Shigeta, A., S. Ito, R. Kaneko, S. Tomida, K. Inoue, H. Kandori, and I. Kawamura. 2018. Long-distance perturbation on Schiff base-counterion interactions by His30 and the extracellular Na(+)-binding site in Krokinobacter rhodopsin 2. *Phys Chem Chem Phys*. 20(13):8450-8455, doi: 10.1039/c8cp00626a.
32. Deisseroth, K. 2011. Optogenetics. *Nat Methods*. 8(1):26-29, doi: 10.1038/nmeth.f.324.'PMICD:' PMC6814250.

33. Zhang, F., J. Vierock, O. Yizhar, L. E. Fenno, S. Tsunoda, A. Kianianmomeni, M. Prigge, A. Berndt, J. Cushman, J. Polle, J. Magnuson, P. Hegemann, and K. Deisseroth. 2011. The microbial opsin family of optogenetic tools. *Cell*. 147(7):1446-1457, doi: 10.1016/j.cell.2011.12.004.'PMICD:' PMC4166436.
34. Maciejko, J., M. Mehler, J. Kaur, T. Lieblein, N. Morgner, O. Ouari, P. Tordo, J. Becker-Baldus, and C. Glaubitz. 2015. Visualizing Specific Cross-Protomer Interactions in the Homo-Oligomeric Membrane Protein Proteorhodopsin by Dynamic-Nuclear-Polarization-Enhanced Solid-State NMR. *J Am Chem Soc*. 137(28):9032-9043, doi: 10.1021/jacs.5b03606.
35. Maresca, J. A., J. L. Keffer, and K. J. Miller. 2016. Biochemical Analysis of Microbial Rhodopsins. *Curr Protoc Microbiol*. 41:1F 4 1-1F 4 18, doi: 10.1002/cpmc.5.'PMICD:' PMC4948119.
36. Stevens, T. J., R. H. Fogh, W. Boucher, V. A. Higman, F. Eisenmenger, B. Bardiaux, B. J. van Rossum, H. Oschkinat, and E. D. Laue. 2011. A software framework for analysing solid-state MAS NMR data. *J Biomol NMR*. 51(4):437-447, doi: 10.1007/s10858-011-9569-2.'PMICD:' PMC3222832.
37. Brown, L. S., L. Bonet, R. Needleman, and J. K. Lanyi. 1993. Estimated acid dissociation constants of the Schiff base, Asp-85, and Arg-82 during the bacteriorhodopsin photocycle. *Biophys J*. 65(1):124-130, doi: 10.1016/S0006-3495(93)81064-6.'PMICD:' PMC1225707.
38. Tsujimura, M., and H. Ishikita. 2021. Identification of intermediate conformations in the photocycle of the light-driven sodium-pumping rhodopsin KR2. *Journal of Biological Chemistry*. 296:100459, doi: 10.1016/j.jbc.2021.100459.'PMICD:' PMC8039564.
39. Mobius, K., S. Kazemi, P. Guntert, A. Jakob, A. Heckel, J. Becker-Baldus, and C. Glaubitz. 2019. Global response of diacylglycerol kinase towards substrate binding observed by 2D and 3D MAS NMR. *Sci Rep*. 9(1):3995, doi: 10.1038/s41598-019-40264-8.'PMICD:' PMC6408475.
40. Paramasivam, S., C. L. Suiter, G. Hou, S. Sun, M. Palmer, J. C. Hoch, D. Rovnyak, and T. Polenova. 2012. Enhanced sensitivity by nonuniform sampling enables multidimensional MAS NMR spectroscopy of protein assemblies. *J Phys Chem B*. 116(25):7416-7427, doi: 10.1021/jp3032786.'PMICD:' PMC3386641.
41. Bostock, M., and D. Nietlispach. 2017. Compressed sensing: Reconstruction of non-uniformly sampled multidimensional NMR data. *Concepts in Magnetic Resonance Part A*. 46A(2), doi: 10.1002/cmr.a.21438.
42. Pauli, J., M. Baldus, B. van Rossum, H. de Groot, and H. Oschkinat. 2001. Backbone and side-chain 13C and 15N signal assignments of the alpha-spectrin SH3 domain by magic angle spinning solid-state NMR at 17.6 Tesla. *ChemBioChem*. 2(4):272-281, doi: 10.1002/1439-7633(20010401)2:4<272::AID-CBIC272>3.0.CO;2-2.
43. Shi, L., M. A. Ahmed, W. Zhang, G. Whited, L. S. Brown, and V. Ladizhansky. 2009. Three-dimensional solid-state NMR study of a seven-helical integral membrane proton pump--structural insights. *J Mol Biol*. 386(4):1078-1093, doi: 10.1016/j.jmb.2009.01.011.
44. Luca, S., D. V. Filippov, J. H. van Boom, H. Oschkinat, H. J. de Groot, and M. Baldus. 2001. Secondary chemical shifts in immobilized peptides and proteins: a qualitative basis for structure refinement under magic angle spinning. *J Biomol NMR*. 20(4):325-331, doi: 10.1023/a:1011278317489.
45. Suomivuori, C. M., A. P. Gamiz-Hernandez, D. Sundholm, and V. R. I. Kaila. 2017. Energetics and dynamics of a light-driven sodium-pumping rhodopsin. *Proc Natl Acad Sci U S A*. 114(27):7043-7048, doi: 10.1073/pnas.1703625114.'PMICD:' PMC5502629.
46. Maciejko, J., J. Kaur, J. Becker-Baldus, and C. Glaubitz. 2019. Photocycle-dependent conformational changes in the proteorhodopsin cross-protomer Asp-His-Trp triad revealed by DNP-enhanced MAS-NMR. *Proc Natl Acad Sci U S A*. 116(17):8342-8349, doi: 10.1073/pnas.1817665116.'PMICD:' PMC6486740.
47. Bergo, V. B., O. A. Sineshchekov, J. M. Kralj, R. Partha, E. N. Spudich, K. J. Rothschild, and J. L. Spudich. 2009. His-75 in proteorhodopsin, a novel component in light-driven

proton translocation by primary pumps. *Journal of Biological Chemistry*. 284(5):2836-2843, doi: 10.1074/jbc.M803792200.'PMICD:' PMC2631968.
48. Hempelmann, F., S. Holper, M. K. Verhoefen, A. C. Woerner, T. Kohler, S. A. Fiedler, N. Pfleger, J. Wachtveitl, and C. Glaubitz. 2011. His75-Asp97 cluster in green proteorhodopsin. *J Am Chem Soc*. 133(12):4645-4654, doi: 10.1021/ja111116a.
49. Otomo, A., M. Mizuno, K. Inoue, H. Kandori, and Y. Mizutani. 2020. Allosteric Communication with the Retinal Chromophore upon Ion Binding in a Light-Driven Sodium Ion-Pumping Rhodopsin. *Biochemistry*. 59(4):520-529, doi: 10.1021/acs.biochem.9b01062.
50. Zhang, J., C. N. Kriebel, Z. Wan, M. Shi, C. Glaubitz, and X. He. 2022. Automated Fragmentation Quantum Mechanical Calculation of 15N and 13C Chemical Shifts in a Membrane Protein. *to be submitted*.
51. Leeder, A. J., L. J. Brown, J. Becker-Baldus, M. Mehler, C. Glaubitz, and R. C. D. Brown. 2018. Synthesis of isotopically labeled all-trans retinals for DNP-enhanced solid-state NMR studies of retinylidene proteins. *J Labelled Comp Radiopharm*. 61(13):922-933, doi: 10.1002/jlcr.3576.
52. Shi, C., H. K. Fasshuber, V. Chevelkov, S. Xiang, B. Habenstein, S. K. Vasa, S. Becker, and A. Lange. 2014. BSH-CP based 3D solid-state NMR experiments for protein resonance assignment. *J Biomol NMR*. 59(1):15-22, doi: 10.1007/s10858-014-9820-8.
53. Westfeld, T., R. Verel, M. Ernst, A. Bockmann, and B. H. Meier. 2012. Properties of the DREAM scheme and its optimization for application to proteins. *J Biomol NMR*. 53(2):103-112, doi: 10.1007/s10858-012-9627-4.

Supporting Figures

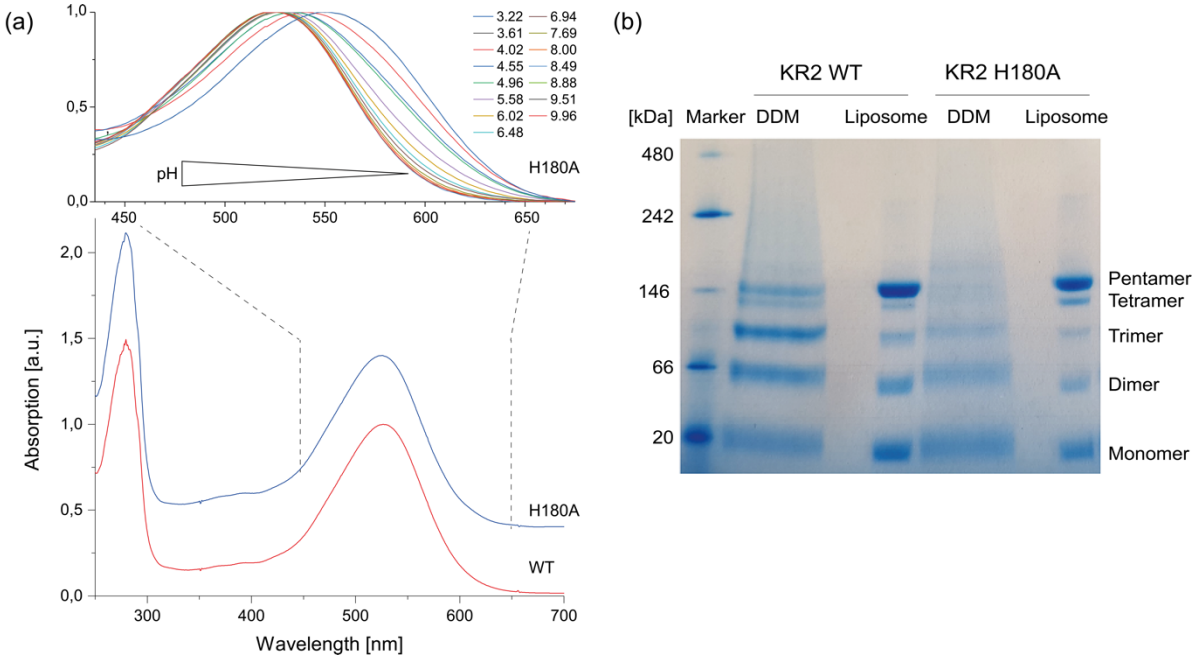

Figure S1: Biochemical characterization of $KR2_{H180A}$. (a) Absorption spectra of KR2 and $KR2_{H180A}$ at pH 8.5 (100 mM NaCl, 0.05% DDM) and pH-dependent shift of the retinal peak for $KR2_{H180A}$ (top). The $KR2_{H180A}$ spectrum has been shifted by 0.5 units for better visualization. A plot of λ_{max} vs. pH is shown in Fig. 1d. **(b)** Blue-native PAGE of KR2 and $KR2_{H180A}$ showing almost equal distribution of oligomers in detergent (E1, 0.05% DDM) but clearly dominating pentameric assembly upon reconstitution. 0.125 % DDM was added to the proteoliposome (PL) sample prior to loading on the gel.

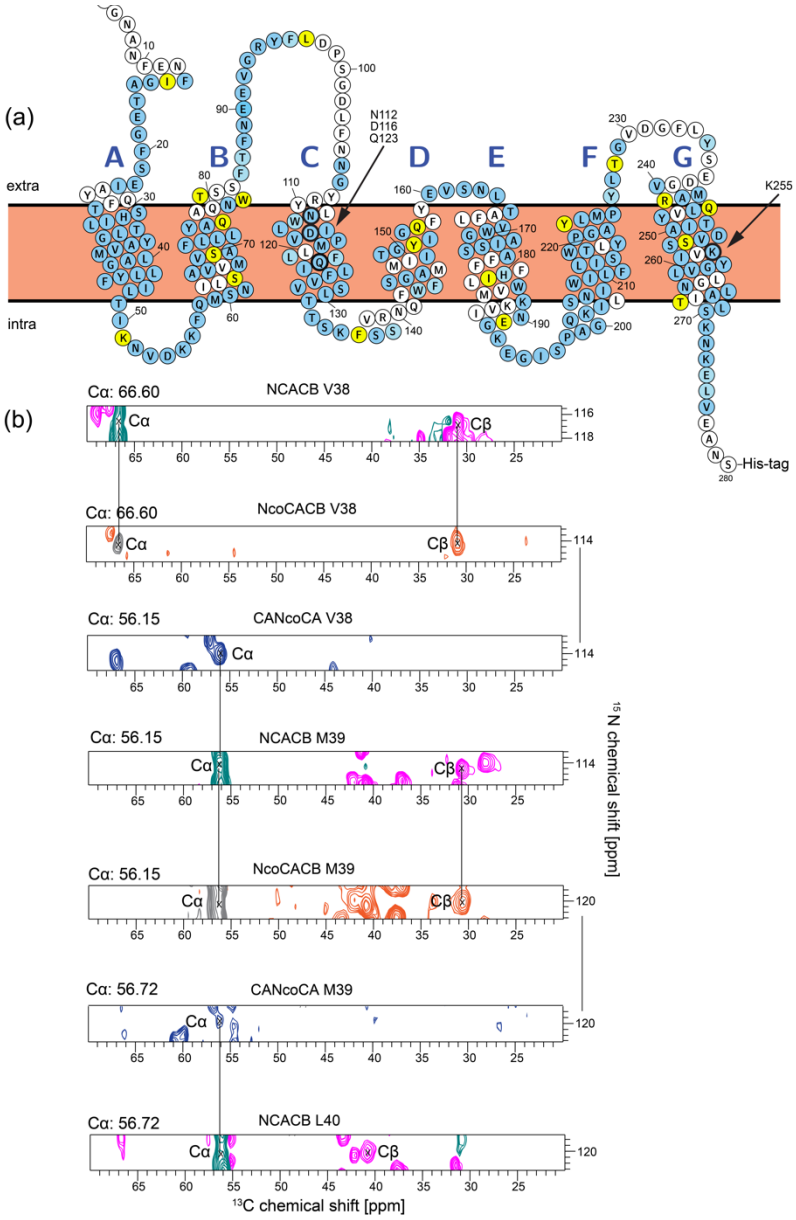

Figure S2: KR2 resonance assignment. (a) KR2 topology plot illustrating the resonance assignment, which covers more than 80% of all sequentially assignable residues (203) including sidechains. Assigned residues are highlighted in blue and summarized in Tab. S1. Highlighted in yellow are those residues affected by the H180A mutation (see Tab. S2) **(b)** Example for sequential backbone and side chain assignment shown here for residues V38 to L40. 2D slices were taken from 3D NCACB, NcoCACB and CANcoCA experiments which allow the identification and linkage of spin systems to each other. Positive and negative phasing of signals are color coded in the DREAM transfer experiments (NCACB, NcoCACB). In NCACB, negatively phased CB signals are indicated in pink, all other, positively phased signals in green. In NcoCACB, red indicates negative and grey positive phasing, respectively. In CANcoCA, inter-carbon magnetization transfer was achieved by BSH-CP (1).

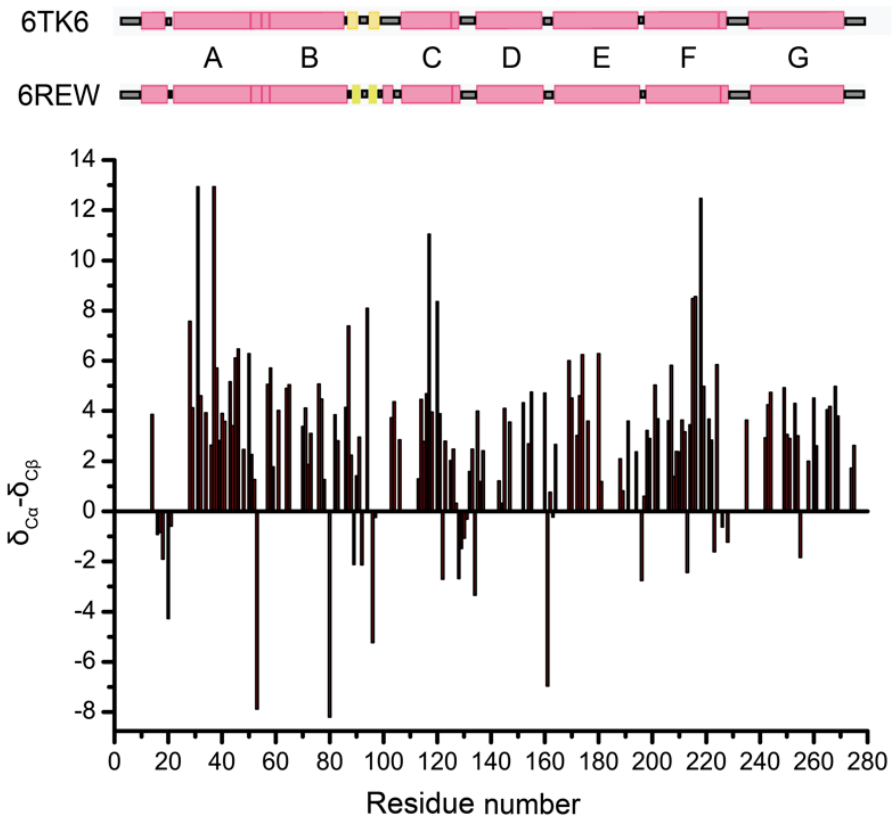

Figure S3: Secondary chemical shift histogram. In the bar plot, positive values indicate alpha helical regions and negative values correspond to non-alpha helical segments (beta sheets, loops). The predicted secondary structures are compared to those found in the monomeric (PDB 6TK6) and pentameric (PDB 6REW) X-ray structures.

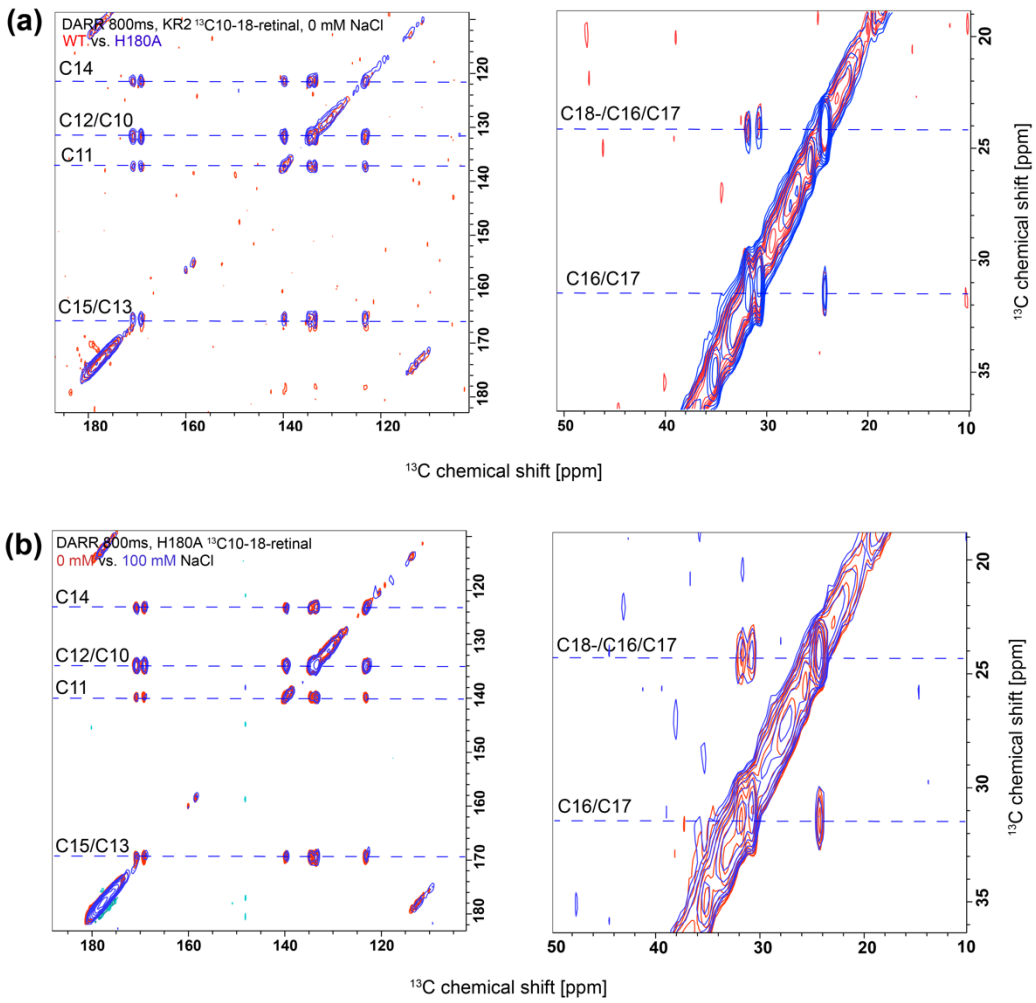

Figure S4: The effect of NaCl and the H180A mutation on the ^{13}C chemical shifts of the retinal chromophore in KR2. **(a)** Comparison between $^{13}C_{10\text{-}18}$-retinal in KR2 (red) and $KR2_{H180A}$ (blue) in the absence of NaCl. **(b)** Comparison between $^{13}C_{10\text{-}18}$-retinal in $KR2_{H180A}$ without (red) and with 100 mM NaCl (blue). Neither the H180A mutation nor the presence of NaCl causes a significant ^{13}C chemical shift change of the retinal carbons (Tab. S3). The spectrum of $^{13}C_{10\text{-}18}$-retinal in KR2 was replotted from (2). The spectra of $^{13}C_{10\text{-}18}$-retinal in $KR2_{H180A}$ were recorded at 850 MHz with a DARR mixing time of 800 ms. For further details on the retinal see (3,4).

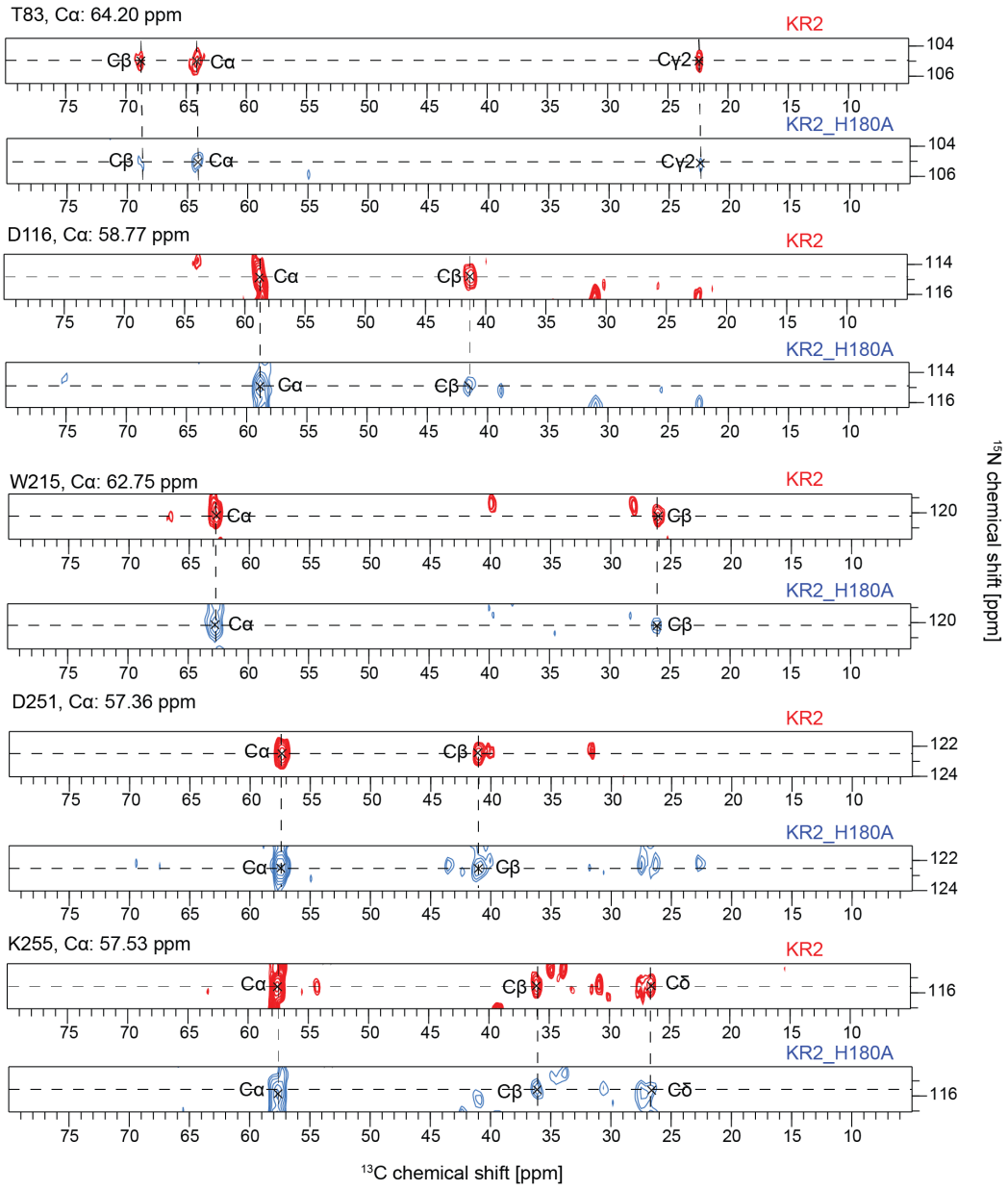

Figure S5: The effect of the H180A mutation on selected functional KR2 residues. Comparison of 2D slices of 3D NCACX spectra of KR2 with KR2$_{H180A}$. Here, a selection of spin systems of functionally relevant residues is shown, which are not affected by the mutation (see also Fig. 3). Slices were taken on [U-^{13}C,^{15}N, rev-FYLIV]-KR2 and [U-^{13}C,^{15}N, rev-FYLIV]-KR2$_{H180A}$. A general summary is provided in Tab. S2.

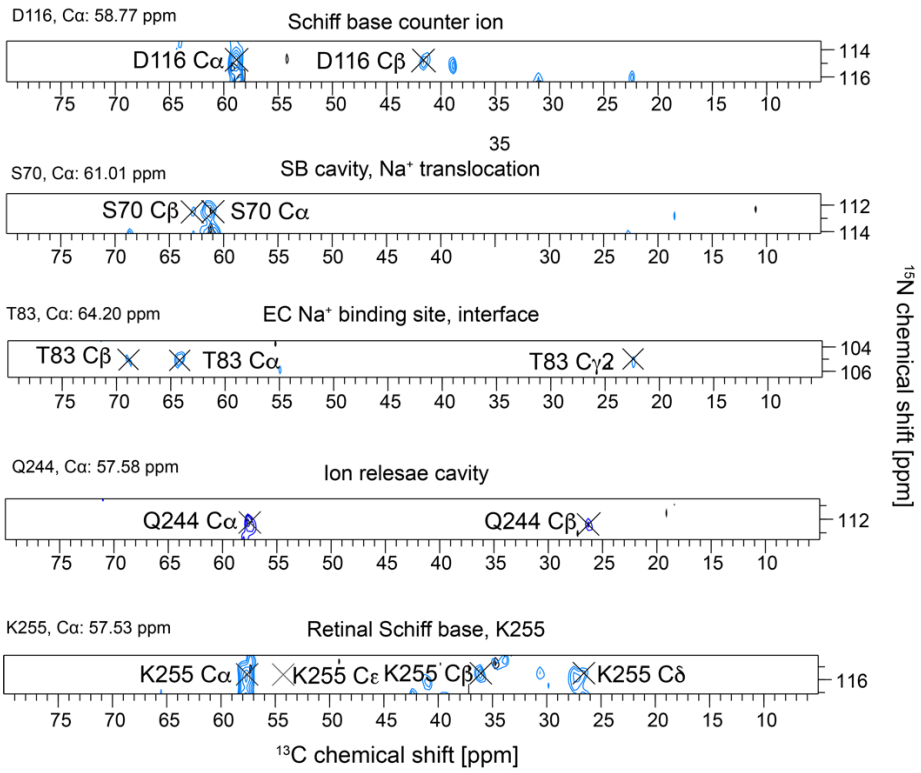

Figure S6: General effects of sodium on KR2$_{H180A}$ spectra. Selected slices of functional spin systems from 3D NCACX spectra of [U-^{13}C, ^{15}N]-KR2$_{H180A}$ recorded without (blue) and with 100 mM NaCl (black). NaCl induced signal losses and chemical shift changes are very similar to the effect on wild type KR2 (Fig. 4b, Tab. S4).

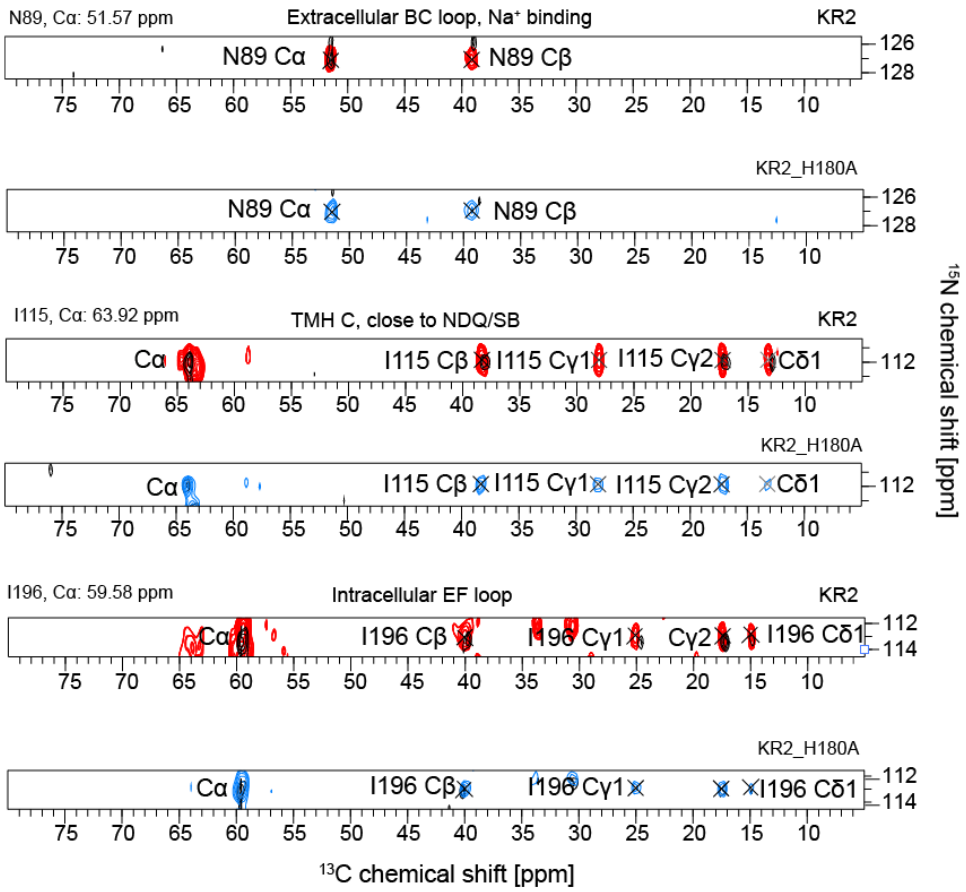

Figure S7: Mutation-specific effects of sodium on KR2$_{H180A}$ spectra. Selected slices from 3D NCACX spectra of [U-^{13}C, ^{15}N]-KR2$_{H180A}$ with (black) and without 100 mM NaCl (blue). [U-^{13}C, ^{15}N]-KR2 (N89 slice taken from [U-^{13}C,^{15}N, rev-FYLIV]-KR2) with (black) and without 100 mM NaCl (red). Only spin systems of those residues are shown, which differ from the wild type in presence of NaCl. All other residues show a similar effect as in wildtype KR2 (Figs. 4b, S6, Tab. S4).

Supporting Tables

Table S1: Summary of assigned KR2 backbone and side chain resonances

All chemical shifts were referenced to DSS via 1-Alanine 13CO. The BMRB access code is: 51639.

Residue	Nuclei							
	N [ppm]	CO [ppm]	Cα [ppm]	Cβ [ppm]	Cɣ [ppm]	Cδ [ppm]	Cε [ppm]	Cζ [ppm]
2Thr	116.25	174.89	65.21	68.21	19.63	-	-	-
13Phe	-	179.74	-	-	-	-	-	-
14Ile	121.17	178.49	61.31	34.59	17.48 26.72	-	-	-
15Gly	106.10	173.52	47.89	-	-	-	-	-
16Ala	120.80	178.27	52.88	20.28	-	-	-	-
17Thr	108.16	174.48	61.42	69.97	21.19	-	-	-
18Glu	121.35	178.31	56.66	31.76	35.84	-	-	-
19Gly	107.71	170.96	43.78	-	-	-	-	-
20Phe	115.71	176.39	56.24	42.19	138.19	131.03*	130.45*	-
21Ser	119.77	174.19	58.16	64.21	-	-	-	-
22Glu	120.64	178.40	60.29	27.59	-	-	-	-
23Ile	119.37	-	-	-	-	-	-	-
28Thr	113.49	174.74	66.95	67.52	18.98	-	-	-
29Ser	113.76	177.24	61.47	62.74	-	-	-	-
30His	122.42	-	57.07	-	-	-	-	-
31Ile	118.64	178.98	66.40	-	-	-	-	-
32Leu	118.22	178.06	57.39	39.81	-	25.29	-	-
33Thr	114.33	175.15	67.67	-	21.96	-	-	-
34Leu	122.57	178.22	57.72	40.65	27.47	26.12 22.76	-	-
35Gly	102.22	174.69	48.39	-	-	-	-	-
36Tyr	117.43	176.04	60.69	39.16	-	-	-	-
37Ala	118.90	179.13	57.69	18.10	-	-	-	-
38Val	116.74	177.64	66.60	30.98	23.68 23.02	-	-	-
39Met	114.46	178.69	56.15	30.72	33.76	-	-	-
40Leu	120.39	177.98	56.78	40.03	26.57	25.54 22.53	-	-
41Ala	121.28	179.61	55.40	17.95	-	-	-	-
42Gly	105.19	174.12	46.54	-	-	-	-	-
43Leu	122.54	177.02	59.54	41.09	27.05	25.31	-	-
44Leu	116.28	177.49	57.75	40.77	26.69	-	-	-
45Tyr	118.73	178.20	63.11	37.91	-	-	-	-
46Phe	118.00	178.34	62.52	38.49	138.88	131.60	130.72 130.08	129.04
47Ile	116.46	177.95	65.07	-	28.78 17.43	14.43	-	-
48Leu	-	178.25	56.87	41.61	26.65	21.78	-	-
49Thr	104.69	176.24	61.41	69.50	21.62	-	-	-
50Ile	125.00	175.07	66.97	38.54	31.04 17.37	15.52	-	-
51Lys	110.90	176.82	56.32	30.73	25.15	-	-	-

52Asn	117.76	174.30	53.55	37.92	176.74	-	-	-
53Val	109.27	175.18	58.21	36.04	22.79 18.12	-	-	-
54Asp	120.88	-	55.12	-	-	-	-	-
55Lys	-	178.37	-	-	-	-	-	-
56Lys	115.82	-	-	-	-	-	-	-
57Phe	114.10	178.21	62.43	39.20	-	-	-	-
58Gln	120.36	177.08	59.41	27.12	35.28	179.93	-	-
59Met	116.19	177.81	55.72	30.88	-	-	-	-
60Ser	110.42	176.47	62.72	-	-	-	-	-
61Asn	117.51	175.72	57.82	39.19	177.14	-	-	-
64Ser	116.82	175.31	61.93	62.54	-	-	-	-
65Ala	123.16	177.85	55.72	17.42	-	-	-	-
66Val	118.57	-	63.19	-	-	-	-	-
68Met	118.09	178.89	57.18	34.87	33.63	-	-	-
69Val	118.19	176.66	67.24	-	21.31	-	-	-
70Ser	112.64	176.91	61.02	62.89	-	-	-	-
71Ala	-	-	54.98	17.02	-	-	-	-
72Phe	118.51	179.08	60.11	39.94	-	-	-	-
73Leu	120.12	177.79	57.46	41.66	26.32	22.08	-	-
74Leu	120.06	173.84	57.37	-	-	23.17	-	-
75Leu	120.37	176.79	59.39	-	-	-	-	-
76Tyr	-	177.45	60.60	36.51	-	-	-	-
77Ala	128.15	178.99	55.49	17.95	-	-	-	-
78Gln	113.96	179.78	56.21	28.31	32.30	-	-	-
81Asn	118.95	178.07	55.21	-	-	-	-	-
82Trp	122.90	176.42	61.36	28.86	110.41	-	-	-
83Thr	105.02	177.81	64.22	69.01	22.44	-	-	-
86Phe	117.02	176.72	59.98	37.17	-	-	-	-
87Thr	115.21	175.15	67.82	68.35	20.05	-	-	-
88Phe	131.33	173.65	59.74	39.17	-	-	-	-
89Asn	126.95	174.77	51.57	39.23	176.14	-	-	-
90Glu	125.16	176.72	58.16	29.83	-	177.67	-	-
91Glu	119.13	177.54	58.76	29.34	36.57	-	-	-
92Val	112.70	176.23	61.72	33.97	21.51 20.89	-	-	-
93Gly	110.07	173.72	46.84	-	-	-	-	-
94Arg	113.92	173.45	53.77	36.06	28.29	43.48	-	-
95Tyr	119.91	-	58.30	-	-	-	-	-
96Phe	118.48	176.14	56.07	43.43	140.28	132.21	-	-
97Leu	122.02	175.41	55.55	43.19	26.68	-	-	-
106Asn	122.53	175.41	55.46	36.97	179.46	-	-	-
107Gly	106.49	-	-	-	-	-	-	-
112Asn	-	177.46	-	37.18	-	-	-	-
113Trp	118.67	176.77	57.46	28.02	113.48			
114Leu	118.98	176.03	57.67	40.45	26.77	22.48	-	-
115Ile	111.88	178.69	63.92	38.36	28.13 17.25	13.26	-	-
116Asp	114.86	175.00	58.77	41.35	177.07	-	-	-

117Val	114.90	175.05	68.16	28.88	24.86	-	-	-
118Pro	131.25	179.75	66.50	31.39	28.30	50.25	-	-
119Met	114.28	177.52	57.18	34.85	33.82	-	20.42	-
121Leu	116.86	175.62	56.54	39.55	25.88	21.98	-	-
122Phe	112.89	179.56	56.44	41.18	139.04	-	131.05	-
123Gln	112.27	177.18	59.38	30.58	33.61	179.22	-	-
124Ile	117.64	176.65	64.54	-	15.59	14.18	-	-
125Leu	118.65	177.07	55.03	40.15	26.57	24.92 22.08	-	-
126Phe	115.16	174.05	59.19	38.89	140.33	131.99	-	127.84
127Val	117.23	174.92	64.06	34.45	22.21 21.42	-	-	-
128Val	108.47	175.59	60.09	33.03	22.64 18.00	-	-	-
129Ser	118.33	172.15	57.36	64.28	-	-	-	-
130Leu	120.87	177.96	53.65	41.72	26.64	25.21 22.41	-	-
131Thr	114.43	175.30	60.77	68.59	22.71	-	-	-
132Thr	116.97	175.99	63.02	69.63	21.75	-	-	-
133Ser	122.58	171.54	59.79	62.51	-	-	-	-
134Lys	120.46	176.27	54.54	33.89	24.89	-	-	-
135Phe	125.65	175.35	61.87	39.29	-	-	-	-
136Ser	113.27	175.49	61.89	66.38	-	-	-	-
137Ser	114.31	176.63	60.46	63.27	-	-	-	-
143Trp	118.23	176.55	58.56	29.16	-	-	-	-
144Phe	121.55	176.22	57.19	39.46	-	-	-	-
145Ser	-	176.96	62.36	63.26	-	-	-	-
146Gly	110.14	173.84	47.68	-	-	-	-	-
147Ala	122.42	179.32	55.28	17.95	-	-	-	-
151Ile	-	177.41	-	38.19	17.20	-	-	-
152Thr	107.36	177.10	65.79	69.00	23.63	-	-	-
153Gly	108.44	173.93	47.93	-	-	-	-	-
154Tyr	122.63	176.39	60.13	38.33	-	-	-	-
155Ile	116.24	177.75	65.45	38.13	15.59	14.10	-	-
156Gly	102.52	177.63	49.21	-	-	-	-	-
157Gln	115.20	177.87	58.20	-	34.43	179.66	-	-
160Glu	-	-	58.23	27.20	-	-	-	-
161Val	119.06	176.47	62.35	-	-	-	-	-
162Ser	115.61	175.71	60.29	64.64	-	-	-	-
163Asn	120.59	172.90	53.25	38.74	177.63	-	-	-
164Leu	127.23	178.02	57.66	41.66	27.34	26.44	-	-
165Thr	119.94	-	67.68	-	-	-	-	-
169Val	-	-	67.49	31.08	-	-	-	-
170Trp	117.96	178.78	61.22	28.70	-	126.86	-	113.14
171Gly	103.94	175.09	47.36	-	-	-	-	-
172Ala	127.25	178.74	55.26	18.22	-	-	-	-
173Ile	118.55	176.69	65.76	38.26	28.64	14.03	-	-
174Ser	112.45	179.04	63.05	63.94	-	-	-	-
175Ser	113.75	174.52	62.63	-	-	-	-	-

176Ala	124.92	178.65	55.85	18.01	-	-	-	-
180His	119.64	178.07	60.84	28.91	-	-	-	-
181Ile	119.43	177.86	61.13	37.09	19.14	-	-	-
183Trp	117.44	177.87	59.43	35.23	112.49	-	-	-
186Lys	-	177.31	-	-	-	-	-	-
190Asn	120.72	177.20	55.06	-	-	-	-	-
191Glu	121.87	179.43	60.07	29.60	37.03	183.45	-	-
192Gly	107.65	174.56	46.14	-	-	-	-	-
193Lys	115.46	177.94	58.01	30.74	-	-	-	-
194Glu	118.10	178.12	58.07	28.95	36.00	183.74	-	-
195Gly	110.54	174.52	45.74	-	-	-	-	-
196Ile	113.05	175.41	59.58	40.02	25.09 17.51	14.96	-	-
197Ser	116.78	173.09	56.92	63.08	-	-	-	-
198Pro	135.93	179.25	65.82	31.73	28.03	50.28	-	-
199Ala	119.17	180.85	55.02	18.24	-	-	-	-
200Gly	107.11	175.22	47.00	-	-	-	-	-
201Gln	121.08	178.46	60.29	27.83	34.70	-	-	-
202Lys	119.88	178.47	59.27	32.09	24.88	-	-	-
203Ile	118.74	-	65.55	-	18.59	13.13	-	-
205Ser	-	176.48	62.33	-	-	-	-	-
206Asn	121.96	174.19	55.79	37.47	177.16	-	-	-
207Ile	121.41	176.84	66.37	37.19	-	14.34	-	-
208Trp	119.38	175.60	59.27	29.86	110.90	127.52	-	-
209Ile	115.66	-	64.32	37.59	18.38	12.70		
210Leu	-	179.19	58.33	42.67	27.08	-	-	-
211Phe	124.42	174.34	61.48	39.84	137.20	-	-	129.15
212Leu	117.55	-	57.85	42.04	26.56	-	-	-
213Ile	114.93	176.68	58.74	38.27	28.92 16.96	14.58	-	-
214Ser	111.86	176.44	63.13	64.59	-	-	-	-
215Trp	120.19	178.80	62.73	26.12	-	-	-	115.06
216Thr	115.17	174.47	67.43	66.58	23.22	-	-	-
218Tyr	115.41	178.31	65.37	35.17	-	-	-	-
219Pro	137.27	177.87	64.74	29.09	26.61	49.36	-	-
220Gly	105.86	173.92	47.89	-	-	-	-	-
221Ala	121.38	179.32	55.21	17.80	-	-	-	-
222Tyr	122.26	176.06	61.73	39.59	-	-	-	-
223Leu	112.20	177.17	55.43	44.76	26.93	22.75	-	-
224Met	117.45	171.54	59.10	31.54	29.28	-	-	-
225Pro	129.60	-	64.80	-	-	49.53	-	-
226Tyr	108.60	177.60	58.29	39.85	131.33	-	-	-
227Leu	-	174.15	57.56	-	-	-	-	-
228Thr	99.60	174.46	59.00	67.73	23.18	-	-	-
229Gly	107.02	-	43.89	-	-	-	-	-
235Tyr	125.12	175.26	57.73	34.70	-	-	-	-
240Val	-	-	67.47	-	-	-	-	-
241Met	117.34	177.93	59.13	34.94	-	-	-	-
242Ala	118.42	178.71	55.44	18.92	-	-	-	-

243Arg	116.93	176.37	60.87	31.31	27.68	45.42	-	-
244Gln	111.98	178.78	57.44	26.36	32.41	-	-	-
245Leu	121.91	178.78	58.67	-	26.19	23.35	-	-
247Tyr	-	-	58.66	-	-	-	-	-
248Thr	114.82	175.91	68.09	-	19.91	-	-	-
249Ile	120.72	178.80	65.74	38.40	28.79 17.07	13.56	-	-
250Ala	125.61	180.10	55.68	19.17	-	-	-	-
251Asp	122.56	176.80	57.36	41.02	180.08	-	-	-
252Val	118.06	178.85	67.25	-	22.36 21.02	-	-	-
253Ser	115.54	174.17	63.26	64.07	-	-	-	-
254Ser	115.80	175.37	61.22	63.56	-	-	-	-
255Lys	115.61	178.00	57.53	36.09	-	26.58	51.59	-
257Ile	-	177.66	-	-	-	-	-	-
258Tyr	119.28	175.15	61.39	40.26	-	-	-	-
259Gly	103.52	177.55	48.30	-	-	-	-	-
260Val	125.30	178.56	66.50	31.98	23.42 22.53	-	-	-
261Leu	120.00	-	57.01	41.47	-	-	-	-
264Asn		175.42	55.31	-	-	-	-	-
265Leu	125.50	177.69	57.77	40.54	27.29	26.42 23.44	-	-
266Ala	122.65	177.94	55.11	17.33	-	-	-	-
268Thr	115.18	175.84	66.15	68.89	21.39	-	-	-
269Leu	-	178.33	58.21	41.69	27.74	-	-	-
270Ser	115.51	176.62	62.46	-	-	-	-	-
271Lys	117.85	176.04	59.17	-	23.11	-	43.56	-
272Asn	115.53	175.80	55.95	37.16	-	-	-	-
273Lys	108.88	-	-	-	-	-	-	-
274Glu	122.41	178.05	58.79	30.52	34.76	179.83	-	-
275Leu	122.40	177.89	57.69	42.31	-	-	-	-
276Val	116.19	-	-	-	-	-	-	-

(*) indicates not unambiguously assignable Cδ and Cε 20Phe resonances due to very close chemical shifts.

Table S2: Summary of KR2 residues affected by the H180A mutation (see Figs. 5, S2a)

Residues affected in $KR2_{H180A}$	
TMH / Loop	**Residue**
N-terminus	I14*
A	none
AB	K51
B	S64, S70, Q78
BC	W82, T83, L97*
C	-
CD	F135*
D	Y154, Q157
DE	-
E	I181
EF	E191*
F	Y222
FG	T228
G	R243, Q244, S253, T268*
C-terminus	-

(*) indicates partial signal loss; all other fully lost.

Table S3: Summary of ^{13}C retinal chemical shifts of KR2 and $KR2_{H180A}$ (see Fig. S4)

Retinal ^{13}C chemical shifts [ppm]								
	C10	C11	C12	C13	C14	C15	C16/C17	C18
KR2*	134.2	139.2	133.1	170.5	122.7	168.7	31.5/30.5	23.7
$KR2_{H180A}$	135.3	139.5	135.3	170.8	123.1	169.0	31.3	24.0

All chemical shifts are referenced to DSS via 1-Alanine 13CO.

(*) as previously reported (2)

Table S4: Summary of sodium-induced effects on 3D NCACX spectra of KR2 and $KR2_{H180A}$ (see Figs. 4, S6, S7)

Experimental Conditions: Spectra were recorded on KR2 proteoliposomes washed and incubated multiple times in a total volume of 15 ml 100 mM NaCl containing NMR buffer (25 mM HEPES, 5 mM $MgCl_2$ at pH 8.5). During the last washing step, resuspended sample was illuminated with green light under mild stirring to ensure photocycle activation.

Nr.	Affected residue	KR2	$KR2_{H180A}$
1	I14	x	x
2	F20	x	x
3	S21	x	x
4	E22	-	Cγ x
5	I31	x	x
6	Y36	x	x
7	M39	x	x
8	L40	x	x
9	G42	x	x
10	L44	x	x
11	Y45	x	x
12	K51	x	x
13	F57	x	x
14	N61	Cβ shifted	Cβ x
15	S64	x	x
16	S70	x	x
17	F72	x	x
18	L73	x	x
19	L74	x	x
20	L75	x	x
21	Y76	x	x
22	N78	Cγ shifted, Cβ x	-
23	W82	x	x
24	T83	x	x
25	F86	x	x
26	T87	x	x
27	F88	x	x
28	N89	Only Cα present	-
29	E90	x	x
30	E91	x	x
31	G93	x	x
32	R94	x	x
33	F96	x	x
34	L97	x	x
35	W113	x	x
36	I115	Cγ1 x	Cδ1 x
37	D116	x	x
38	V128	Cγ2 shifted	-
39	L130	x	x
40	S133	-	x
41	K134	x	x
42	F135	x	x

43	F137	x	x
44	F144	x	x
45	G146	x	x
46	Y154	x	x
47	V161	x	x
48	S162	x	x
49	N163	x	x
50	L164	x	x
51	W170	x	x
52	G171	x	x
53	I173	Cγ2+Cδ shifted	shifted
54	A176	x	x
55	H180	x	x
56	I181	x	x
57	E191	Cγ x	Cγ x
58	G192	x	x
59	G195	Very weak	x
60	I196	shifted	Cβ shift, others x
61	G200	Very weak	x
62	K202	x	x
63	I203	Cγ2 x	Cγ2 x
64	I209	x	x
65	L212	x	x
66	I213	Cβ x	Cβ x
67	T216	x	x
68	Y218	x	x
69	Y222	x	x
70	L223	x	x
71	Y226	x	x
72	T228	x	x
73	Q244	x	x
74	L245	x	x
75	D251	x	x
76	S253	x	x
77	K255	x	x
78	L265	Cγ x	Cγ x
79	T268	x	x
80	N272	x	x
81	E274	x	x
82	L275	x	x

All chemical shifts are referenced to DSS via the ^{3}CO resonance of 1-^{13}C Alanine.

'x' indicates a fully disappeared and '-' a non-affected spin system.

If only partially affected, the affected atom is specified.

Table S5: Experimental NMR parameters

- For experimental parameters of NCACX, NCOCX, CONCA experiments see (2).
- All NMR experiments were carried out on KR2 samples at pH 8.5 and at 275 K.
- NCACX spectra on 100 mM NaCl containing KR2 samples were recorded at 265 K to compensate for salt-induced heating effects during NMR pulsing.
- Selective CC magnetization transfer was achieved by DREAM (CA-CB) (5) and BSH-CP (CO-CA) (1) magnetization transfer steps.

Experiment	**^{15}N-CP**			**DARR**		**NCA**	**NCO**	**NCACX**	**NCACX**	
Figure	**4a**			**S4**		**2a**	**2a**	**2b, 3b***	**4b, 5b; S5, S6, S7**	**5b;S5,S6,S7**
Dimensionality	1D			2D		1D	1D	3D	3D	3D
Sample	[U-^{13}C,^{15}N]-KR2 (0 mM)	[U-^{13}C,^{15}N]-KR2$_{H180A}$ (0 mM)	[U-^{13}C,^{15}N]-KR2 (100 mM NaCl) or [U-^{13}C,^{15}N]-KR2$_{H180A}$ (100 mM NaCl)	$^{13}C_{10-18}$-retinal KR2$_{H180A}$ 0 mM NaCl/100 mM NaCl		[U-^{13}C,^{15}N]-KR2	[U-^{13}C,^{15}N]-KR2	[U-^{13}C,^{15}N, rev-FYLIV]-KR2, [U-^{13}C,^{15}N]-KR2	[U-^{13}C,^{15}N]-KR2 (100 mM NaCl) or [U-^{13}C,^{15}N]-KR2$_{H180A}$ (100 mM NaCl)	[U-^{13}C,^{15}N]-KR2$_{H180A}$ (0 mM)
Magnetic field [MHz]/MAS[kHz]	850/14	900/16.5	850/14	850/ 14		900/ 20	900/ 20	850/ 14	850/ 14	900/16.5
Probehead	HCN	E-free	E-free	E-Free		E-free	E-free	E-free	E-Free	E-Free
Recycle delay [s]	3	2	1	1		2	2	0.8	1 (WT) or 1.5 (H180A)	2
Transfer 1 Field [kHz] Shape (ramp) Contact time [ms] Carrier [ppm]	HN-CP 52.2(H) 41.7(N) 80.100 (H) 2.5 120	HN-CP 64.9(H) 41.7(N) 80.100 (H) 1 120	HN-CP 70.6(H) 41.7(N) 80.100 (H) 1.5 120	HC-CP 83.3 (H) 55.5(C) 80.100 (H) 1 99.73	HC-CP 84.6 (H) 55.5(C) 80.100 (H) 1 99.73	HN-CP 82.8(H) 41.7(N) 80.100 (H) 1.2 120	HN-CP 82.8(H) 41.7(N) 80.100 (H) 1.2 120	HN-CP 68.0 (H) 41.7(N) 80.100 (H) 1 113.2	HN-CP 73.2(H) 41.7(N) 80.100 (H) 1.2 120	HN-CP 82.8(H) 41.7(N) 80.100 (H) 1.2 120
Transfer 2 Field [kHz] Shape (ramp)				DARR 14 (H) - 800	DARR 14 (H) - 800	NCA-DCP 49.6(N) 33.8(C) 83.3(H) Ocean_r21 20 kHz (C), (N)	NCO-DCP 49.6(N) 74.7(C) 83.3(H)	NCA-DCP 35.35(N) 22.26(C) 83.3(H)	NCA-DCP 36.8(N) 29.7(C) 83.3(H)	NCA-DCP 49.6(N) 33.8(C) 83.3(H)

Contact/mixing time [ms] Carrier [ppm]				100.1	100.1	3.5 60	Ocean_r3 20 kHz (C), (N) 3.5 177	90.100 (C) 6 55.0	tmSPICE 14 kHz (C), (N) 90.100 (C) 3.495 56	tmSPICE 16.5 kHz (C), (N) 3.5 60
Transfer 3 Field [kHz] Shape (ramp) Contact/mixing time [ms] Carrier [ppm]								DARR 14 (H) - 50 59.4	DARR 14 (H) - 50 54	DARR 14 (H) - 50 54
Transfer 4 Field [kHz] Shape (ramp) Contact/mixing time [ms] Carrier [ppm]										
T1 increments Sweep width [kHz] Acqu. Time [ms]	1732 34.7 25	832 27.8 15	1038 26 20	500 55.6 4.5		2726 91 15	2726 91 15	70 3.5 10.0	70 3.5 10	70 3.3 10
T2 increments Sweep width [kHz] Acqu. Time [ms]				3988 100 20				98 7 7.0	98 7 7.0	98 8.3 6
T3 increments Sweep width [kHz] Acqu. Time [ms]				-				2548 85 15	2548 85 15	2548 90.1 10
T4 increments Sweep width [kHz] Acqu. Time [ms]				-					-	

^{1}H SPINAL decoupling [kHz]	83.3	83.3	83.3	83.3	83.3	83.3	83.3	83.3	83.3	83.3
Number of scans	20480	16000	16000	704	280	32	32	112	80	96
Total measurement time	17h	9h	4.5h	7d	3d	1.5h	1.5h	7d (fully sampled) or 4.5d (65% NUS)	4.5d (WT) 6.2d (H180A) (both 65% NUS)	6d (65% NUS)

(*) 2D NCA spectrum, but same conditions as described here.

Experiment	**NCACB**	**N(CO)CACB**	**CANcoCA**
Figure	**S2b**	**2c, S2b**	**S2b**
Dimensionality	3D	3D/4D	3D
Sample	[U-^{13}C,^{15}N, rev-FYLIV]-KR2, [U-^{13}C,^{15}N]-KR2	[U-^{13}C,^{15}N]-KR2	[U-^{13}C,^{15}N, rev-FYLIV]-KR2, [U-^{13}C,^{15}N]-KR2
Magnetic field [MHz]/MAS[kHz]	850/ 14	850/ 14	900/ 20
Probehead	E-Free	E-Free	E-Free
Recycle delay [s]	0.8	1	2
Transfer 1 Field [kHz] Shape (ramp) Contact time [ms] Carrier [ppm]	HN-CP 67.1 (H) 41.7(N) 80.100 (H) 1 107.9	HN-CP 68.4 (H) 41.6(N) 80.100 (H) 1 107.9	HC-CP 82.8 (H) 55.5(C) 80.100 (H) 1.2 59.63
Transfer 2 Field [kHz] Shape (ramp) Contact/mixing time [ms] Carrier [ppm]	NCA-DCP 38.8(N) 21.7(C) 83.3(H) 90.100 (C) 5.5 46.8	NCO-DCP 38.81(N) 50.56(C) 83.3(H) 90.100 (H) 5 163.69	CAN-DCP 57.02(N) 54.16(C) 83.3(H) t-inv r21 OCean 20 kHz (C),(N) 90.100 (H) 3.5 117.29

Transfer 3 Field [kHz] Shape (ramp) Contact/mixing time [ms] Carrier [ppm]	DREAM 7.34 (H) 70.100 (H) 2.5 46.8	BSH-CP 3.51 (C) 65.100 (H) 4 60.2		NCO-DCP 30.94(N) 34.25(C) 83.3(H) OCean NCO r3, 20 kHz (C),(N) 90.100 (H) 3.5 180.1
Transfer 4 Field [kHz] Shape (ramp) Contact/mixing time [ms] Carrier [ppm]		DREAM 7.83 (C) 70.100 (H) 2.5 46.8		BSH-CP 10.70 (C) 70.100 (H) 5 60
T1 increments Sweep width [kHz] Acqu. Time [ms]	70 3.5 10	57 8	16 3	82 6.2
T2 increments Sweep width [kHz] Acqu. Time [ms]	95 7	80 6	16 2.3	56 8.4
T3 increments Sweep width [kHz] Acqu. Time [ms]	3400 20	2538 15	16 2.3	2726 15
T4 increments Sweep width [kHz] Acqu. Time [ms]	-		2548 15	-
^{1}H SPINAL decoupling [kHz] Number of scans Total measurement time	83.3 136 7d	83.3 176 9d	83.3 208 9d (75% NUS	83.3 80 9d

References

1. Shi, C., H. K. Fasshuber, V. Chevelkov, S. Xiang, B. Habenstein, S. K. Vasa, S. Becker, and A. Lange. 2014. BSH-CP based 3D solid-state NMR experiments for protein resonance assignment. *J Biomol NMR*. 59(1):15-22, doi: 10.1007/s10858-014-9820-8.
2. Kaur, J., C. N. Kriebel, P. Eberhardt, O. Jakdetchai, A. J. Leeder, I. Weber, L. J. Brown, R. C. D. Brown, J. Becker-Baldus, C. Bamann, J. Wachtveitl, and C. Glaubitz. 2019. Solid-state NMR analysis of the sodium pump Krokinobacter rhodopsin 2 and its H30A mutant. *J Struct Biol*. 206(1):55-65, doi: 10.1016/j.jsb.2018.06.001.
3. Jakdetchai, O., P. Eberhardt, M. Asido, J. Kaur, C. N. Kriebel, J. Mao, A. J. Leeder, L. J. Brown, R. C. D. Brown, J. Becker-Baldus, C. Bamann, J. Wachtveitl, and C. Glaubitz. 2021. Probing the photointermediates of light-driven sodium ion pump KR2 by DNP-enhanced solid-state NMR. *Sci Adv*. 7(11), doi: 10.1126/sciadv.abf4213.'PMICD:' PMC7954446.
4. Leeder, A. J., L. J. Brown, J. Becker-Baldus, M. Mehler, C. Glaubitz, and R. C. D. Brown. 2018. Synthesis of isotopically labeled all-trans retinals for DNP-enhanced solid-state NMR studies of retinylidene proteins. *J Labelled Comp Radiopharm*. 61(13):922-933, doi: 10.1002/jlcr.3576.
5. Westfeld, T., R. Verel, M. Ernst, A. Bockmann, and B. H. Meier. 2012. Properties of the DREAM scheme and its optimization for application to proteins. *J Biomol NMR*. 53(2):103-112, doi: 10.1007/s10858-012-9627-4.